Aerospace Science and Technology 176 (2026) 112185

Contents lists available at ScienceDirect

Aerospace Science and Technology

journal homepage: www.elsevier.com/locate/aescte

High-fidelity combustion modeling and thermal loads in HTP-kerosene bipropellant thruster

Prakhar Jindal *, Maximilian Pfohl, Jyoti Botchu

Space System Engineering Section, Space Engineering, Faculty of Aerospace Engineering TU Delft. Kluyverweg 1 2629 HS Delft, Netherlands

ARTICLE INFO

Edited by: Cummings Russell.

Keywords:
Green propulsion
High-test hydrogen peroxide
Bipropellant thruster
Transient combustion simulation
Real-gas effects
CFD analysis
Wall thermal loading

ABSTRACT

The urgent need for sustainable propulsion solutions has accelerated the exploration of green bipropellant thrusters using high-test hydrogen peroxide (HTP) with kerosene. In this study, a transient, high-fidelity CFD model coupling droplet-phase dynamics, real-gas behavior, and finite-rate chemical kinetics was developed to simulate the ignition and combustion processes in a coaxial-injected HTP-kerosene thruster. Simulations investigated the impact of oxidizer purity (95 % and 98 %) and mixture ratio variations, targeting a vacuum thrust of 100 N. Results revealed that stoichiometric mixtures with 98 % HTP delivered the most favorable balance of thrust (63.22 N at sea level) and thermal loads, with combustion temperatures aligning within 1 % of CEA predictions. Fuel-rich mixtures exhibited significant inefficiencies, with up to 18 % unburnt kerosene detected at the nozzle exit. Wall temperatures peaked at 3271 K under adiabatic assumptions, exceeding material safety thresholds, highlighting the necessity of advanced thermal management strategies. Observations of flow separation, shock structures, and model-predicted oxygen backflow further reinforced the realism of the simulations. This study advances green propulsion by linking combustion dynamics with structural viability. It provides new insights into propellant formulation, thermal management, and injector optimization for future environmentally compliant engines.

1. Introduction

The pursuit of environmentally friendly and operationally reliable propulsion systems has catalyzed a global shift away from legacy hydrazine-based engines toward green propellants. Central to this paradigm shift is the application of high-test hydrogen peroxide (HTP) as an oxidizer in bipropellant thrusters. Recent regulatory frameworks, such as the European Green Deal, are accelerating demand for low-toxicity, safe propulsion systems throughout the mission lifecycle [1]. The use of hydrogen peroxide, particularly in high concentrations (90–98 %), in conjunction with hydrocarbon-based fuels such as kerosene, offers significant advantages in terms of performance and operational viability. Unlike conventional staged combustion systems that rely on complex catalyst beds for decomposition, unstaged thrusters using HTP facilitate direct injection of both fuel and oxidizer into the combustion chamber. This configuration avoids the need for dedicated catalytic chambers, reducing system weight, increasing reliability, and simplifying the design architecture [2].

The interest in green propellants is driven by the need to replace toxic hydrazine-based systems, historically dominant due to their hypergolicity and storability, with safer alternatives that maintain operational reliability. While candidates such as ammonium dinitramide (ADN) and hydroxylammonium nitrate (HAN) offer reduced toxicity, they often suffer from thermal instability and high freezing points [3]. In contrast, high-test hydrogen peroxide (HTP) provides an optimal tradeoff: it is stable, possesses high density, and yields non-toxic decomposition products (steam and oxygen). Crucially, when paired with kerosene and a catalyst, HTP facilitates hypergolic ignition, eliminating the need for complex ignition systems while avoiding the carcinogenic risks of hydrazine [4]. The decomposition enthalpy of HTP is significantly lower than hydrazine's (-98.2 kJ/mol vs. -235.1 kJ/mol), but the bipropellant combustion of HTP with hydrocarbons compensates this via highly exothermic reactions, producing combustion temperatures exceeding 3200 K. When combined with kerosene ($C_{12}H_{26}$), the overall specific impulse (I_{sp}) for sea-level operation ranges between 230 and 250 s, depending on the chamber pressure and nozzle geometry. These values are competitive with traditional storable systems, especially when one considers the environmental advantages and absence of

* Corresponding author.
E-mail addresses: p.jindal@tudelft.nl, prakharjindal@gmail.com (P. Jindal).

https://doi.org/10.1016/j.ast.2026.112185
Received 30 May 2025; Received in revised form 11 December 2025; Accepted 18 March 2026
Available online 19 March 2026

carcinogenic byproducts.

A comprehensive review by Okninski et al. [5] demonstrated that HTP-kerosene thrusters can achieve high combustion completeness and mechanical integrity under appropriate conditions. Although the SMILE injector project [6] focused on kerolox (liquid oxygen–kerosene), it provided valuable insights into coaxial injector optimization, which are applicable to bipropellant systems such as HTP-kerosene [5]. Further, in a demonstration by Kang et al. [6], a 500 N class HTP-kerosene engine showed stable combustion and good performance metrics, reinforcing the feasibility of this configuration for practical propulsion. Nonetheless, most existing work has focused on steady-state performance testing, often neglecting transient dynamics crucial for start-up sequences, ignition delay, and early-time heat transfer phenomena. In the early phases of engine operation, specifically within the first 10 ms, fluid dynamics, combustion reactions, and wall interactions evolve rapidly, often deviating from steady-state assumptions. For instance, researchers highlight that temperature gradients during the ignition phase can exceed 1400 K within 1 ms, with associated wall heat fluxes surging up to 1800 W/m^2K, challenging material limits and risking thermal shock [7].

Furthermore, while injector configurations have been modeled in prior work [6,8,9], their downstream impact on internal combustion structure, wall temperature distribution, and the stress-strain response of thruster materials such as UHTCMC (Ultra-High Temperature Ceramic Matrix Composites) has remained underexplored. UHTCMC, although highly capable of withstanding localized thermal spikes, exhibits anisotropic thermal conductivities and nonlinear stress responses under mixed thermal and mechanical loading. These factors are critically important in transient regimes where rapid pressure and temperature changes can initiate delamination or microcrack propagation, thereby affecting operational life and reliability [10,11]. There also exists a lack of clarity on the species composition of the exhaust stream during non-equilibrium combustion. Previous studies often assume complete combustion and ideal mixing, resulting in CO_2 and H_2O as the only products considered. However, some previous research shows that under non-equilibrium, finite-rate kinetics, trace levels of CO, CH_4, and unreacted oxygen can be present, particularly at lower oxidizer-to-fuel ratios or during off-nominal startup conditions. These emissions, while minor in quantity, are essential in certifying the thruster under emission regulations applicable to atmospheric or planetary entry applications [12].

While the basic physics and chemistry of HTP-based propulsion are well understood, traditional design methodologies often decouple flow dynamics from chemical kinetics, relying on steady-state assumptions and equilibrium codes (e.g., NASA CEA). These approaches fail to capture transient ignition spikes, finite-rate species evolution, and nonlinear real-gas effects critical to high-pressure kerosene combustion. The primary objective of this study is to bridge that gap by linking combustion dynamics with structural viability. To achieve this, a high-fidelity, transient CFD framework was developed that combines droplet-phase modeling, finite-rate combustion kinetics, and thermal-stress analysis of the thruster structure. Focusing on the full combustion chamber rather than individual components, the simulation captures spray dynamics, ignition, heat release, and wall stresses with high temporal resolution. Structural effects on the chamber, made from UHTCMC materials, are evaluated using von Mises stress formulations, considering challenges posed by additive manufacturing, such as variable thermal conductivity and anisotropy. Exhaust species and heat flux predictions are benchmarked against established models and validated with experimental data. Moreover, as the aerospace sector increasingly adopts additive manufacturing for propulsion hardware, validating thruster wall performance under transient thermal loading becomes even more critical, given the varied thermal conductivities and material anisotropies introduced by manufacturing defects and layer-wise build patterns [13–15]. This study, therefore, lays the groundwork for transitioning HTP-based systems from laboratory experiments to fully operational, flight-ready propulsion modules. It functions as the predictive design component of a broader research initiative, establishing the thermal and structural boundary conditions for experimental campaigns detailed in separate studies.

Table 1
UHTCMC wall properties.

Property	Value
Density	3477 kg/m^3
Specific Heat	661.87 J/kg·K
Thermal Conductivity	30 W/m·K
Wall Thickness	0.005 m
Maximum Allowable Temp	2773 K

2. Physical and combustion modeling

This section presents the physical foundation of the simulation framework, focusing on the geometry of the thruster, the material properties of its components, the behavior of the propellants under high-pressure, and high-temperature combustion conditions. It outlines the design principles behind the combustion chamber, the thermophysical characteristics of hydrogen peroxide and kerosene, and the chemical reaction mechanisms that govern decomposition and combustion. The modeling approach incorporates finite-rate gas-phase reactions, real-gas effects, and variations in oxidizer concentration to closely match realistic operating behavior.

2.1. Geometry and CAD modeling

The chamber features a cylindrical head-end dome, a cylindrical combustion section, a converging throat, and a conical nozzle. The dome facilitates flow recirculation and pressure stabilization near the injector face, while the cylindrical section ensures sufficient residence time for combustion and thermal homogenization before acceleration into the nozzle. The nozzle contour transitions smoothly from the throat to the exit with a designed expansion ratio of 4:1. This expansion was selected to match typical sea-level test conditions while maintaining internal pressure ratios conducive to effective conversion of thermal energy into directed exhaust velocity. The characteristic dimensions used in the geometry are as follows: combustion chamber diameter of 35 mm, throat diameter of 10 mm, and nozzle exit diameter of 22 mm, with a total axial length of 125 mm. These values were selected based on chemical equilibrium calculations and the engine geometries provided by the industry partner in the project. The length-to-diameter ratio of the chamber was maintained above 3.5 to ensure complete vaporization of droplets and minimize wall impingement. Transitional surfaces were filleted to suppress numerical discontinuities in curvature and to avoid artificial separation or eddy formation that could skew wall flux computations.

In contrast to prior studies that focused on injector behavior, this study deliberately omits the detailed injector geometry to isolate downstream combustion and flow effects. The coaxial injector is modeled implicitly through well-defined inlet boundary conditions that reflect its experimentally validated mass flow split and droplet size characteristics. These values were further validated using the droplet Weber number and injection Reynolds number to ensure physical consistency. The wall thickness was set to 5 mm to mimic the structural profile of UHTCMC, the material selected for the chamber. This value was derived from mechanical and thermal trade-offs reported by the research group and is consistent with thermal protection system requirements for green thruster applications.

2.2. Material specification

The combustion chamber walls were assumed to be made from an

Table 2
CEA output for $p_c = 7.5$ bar.

H_2O_2 Purity	Φ	O/F	T_c [K]	$I_{sp,vac}$ [s]	$I_{sp,sl}$ [s]	$\dot{m}$ [10^{-3} kg/s]
98 %	0.90	8.21	2749	273.1	243.4	37.32
	0.95	7.78	2770	275.5	245.1	37.00
	1.00	7.39	2787	277.4	246.5	36.75
	1.05	7.04	2798	278.6	247.8	36.58
	1.10	6.72	2804	279.2	249.0	36.50
95 %	0.90	8.47	2699	270.2	241.2	37.72
	0.95	8.02	2723	272.7	243.0	37.38
	1.00	7.62	2740	274.7	244.4	37.11
	1.05	7.26	2752	275.9	245.8	36.95
	1.10	6.93	2758	276.3	246.9	36.89
90 %	0.90	8.94	2609	264.8	237.1	38.50
	0.95	8.47	2636	267.6	239.1	38.10
	1.00	8.04	2656	269.8	240.6	37.79
	1.05	7.66	2669	270.7	242.1	37.66
	1.10	7.31	2674	270.8	242.7	37.65

UHTCMC containing carbon fibers. While the injector elements were excluded from detailed geometry, the injector plate itself was modeled as a solid boundary (acting as a wall), made of aluminum, to accurately represent the domain interface. This choice was motivated by the need to withstand elevated thermal loads while minimizing structural deformation. The material properties were obtained from the research group's internal database and are listed in Table 1. These values were directly used to define the conduction behavior of the solid regions and to determine stress profiles in structural post-processing.

The gas mixture's thermal properties were defined using temperature-dependent polynomial fits and updated dynamically during the simulation. Properties such as density, viscosity, thermal conductivity, and specific heat were automatically adjusted by the solver as a function of local composition and temperature.

2.3. Propellant variation analysis

2.3.1. Chemical equilibrium analysis (CEA)

In order to assess how changes in hydrogen peroxide concentration influence combustion performance and thermal loading, a numerical study was conducted using the NASA Chemical Equilibrium with Applications (CEA) code. The study focused on the effect of hydrogen peroxide concentration (α), oxidizer-to-fuel ratio (O/F), and equivalence ratio (Φ) on chamber temperature and specific impulse (I_{sp}). The primary goal was to explore how propellant formulation could reduce wall temperature without significantly compromising thrust performance or combustion efficiency. The simulations considered three HTP concentrations, 90 %, 95 %, and 98 %, to reflect a practical range of oxidizer purity used in green bipropellant systems. For each concentration, the equivalence ratio Φ was varied between 0.90 and 1.10 in increments of 0.05, corresponding to mixtures ranging from fuel-lean to slightly fuel-rich. The chamber pressure was also varied between 5 bar and 10 bar, with particular focus on 7.5 bar, the condition closest to the chamber pressure obtained in the CFD simulations (~7.4 bar).

Table 2 summarizes the computed chamber temperatures and vacuum specific impulses ($I_{sp,vac}$) for various HTP concentrations and equivalence ratios, with chamber pressure held at 7.5 bar. These values were generated by running CEA under equilibrium assumptions. Total mass flow $\dot{m}$ is not output by CEA but was calculated from the vacuum specific impulse and the vacuum thrust requirement $F_{vac} = 100$ N according to Eq. (1):

$$I_{sp} = \frac{F}{\dot{m} g_0} \tag{1}$$

It is important to note that values found from CEA serve as an estimate rather than an exact prediction for transient behavior. The code assumes chemical equilibrium whereas the simulation used finite rate chemistry leading to slower reactions. Furthermore, not all propellant properties in CEA are defined for the inlet temperature of around 300 K, so lower values had to be inserted for the analysis to run. Hence, the real inlet enthalpy would be higher. Regarding the chamber temperature, even the highest temperature in Table 2 was only 31 K above the limit temperature (2773 K). Assuming temperature decreases near the wall due to reduced reactions and external cooling, these values suggest the thermal environment is manageable.

2.3.2. Selection of operational points for CFD

CEA results demonstrated that combustion temperature and I_{sp} both increased with higher chamber pressure, higher oxidizer concentration, and higher equivalence ratio (i.e., lower O/F). However, the analysis also revealed that the maximum I_{sp} was not achieved at stoichiometric conditions ($\Phi = 1.0$) but rather at $\Phi \approx 1.10$ to 1.15. This was attributed to the fact that although stoichiometric combustion ensures complete oxidation of fuel, at higher O/F ratios, increased water formation leads to greater evaporation losses, which consumes thermal energy without directly contributing to thrust production. On the other hand, slightly fuel-rich mixtures suppress water formation and improve momentum transfer in the exhaust gases, thereby increasing I_{sp}.

This behavior is shown in Fig. 1, which plots $I_{sp,vac}$ versus

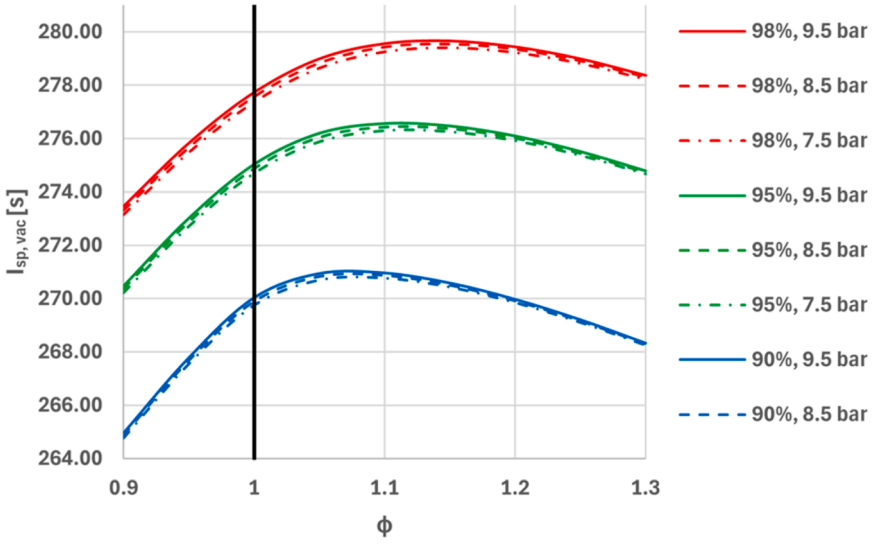

Fig. 1. $I_{sp,vac}$ versus Φ for different concentrations and chamber pressures, obtained from CEA.

equivalence ratio for different HTP concentrations and chamber pressures. The curves clearly indicate that 98 % HTP at $\Phi = 1.10$ yields the highest performance. However, this configuration also results in the highest combustion temperature, exceeding safe thermal limits for the chamber walls. As a compromise between performance and thermal safety, both 95 % and 98 % HTP concentrations were carried forward into the CFD simulations, using equivalence ratios of 1.00 (stoichiometric) and 1.10–1.15 (high-performance case).

Although CEA assumes chemical equilibrium and does not model the reaction time scales involved in real engines, the trends it predicts are valuable for interpreting CFD results and validating combustion behavior under different propellant formulations. CEA outputs were used to benchmark chamber temperatures and guide the selection of mixture ratios in the numerical study.

2.4. Chemical reaction mechanisms and gas modeling

The combustion and decomposition behavior of the hydrogen peroxide–kerosene propellant combination was modeled using a reduced finite-rate chemistry approach, capturing the essential chemical transformations without introducing unnecessary complexity. The detailed decomposition and reaction mechanisms for this hypergolic combination remain not fully resolved in the literature. Several competing pathways have been proposed for hydrogen peroxide decomposition and catalytic reactions, but a consensus mechanism has yet to emerge. Given this lack of clarity and the high computational cost of solving detailed elementary reactions within a transient, three-dimensional framework, a reduced global mechanism was selected. This approach preserves the macroscopic combustion dynamics, specifically the rate of heat release and pressure buildup critical for structural analysis, while maintaining computational feasibility. The reaction mechanism implemented in the simulation consisted of three overall gas-phase reactions:

Thermal decomposition of hydrogen peroxide, Eq. (2):

$$H_2O_2 \rightarrow H_2O + 0.5\ O_2 \tag{2}$$

Catalyst-induced combustion of hydrogen peroxide and kerosene, Eq. (3):

$$C_{12}H_{23} + 35.5\ H_2O_2 \rightarrow 12\ CO_2 + 47\ H_2O \tag{3}$$

Combustion of kerosene with oxygen, Eq. (4):

$$C_{12}H_{23} + 17.75\ O_2 \rightarrow 12\ CO_2 + 11.5\ H_2O \tag{4}$$

These three reactions were specifically selected to decouple the distinct physical pathways governing the transient start-up: Eq. (2) accounts for the thermal decomposition of the oxidizer, Eq. (3) represents the rapid catalyst-driven interaction responsible for ignition initiation, and Eq. (4) captures the bulk gas-phase oxidation of the fuel. While the detailed intermediate steps were not explicitly modeled, this three-reaction framework reflects the net result of the chemical transformations expected in the chamber. All reactions were modeled using finite-rate chemistry, under the assumption that combustion and ignition in this configuration are largely governed by the rate at which hydrogen peroxide decomposes and releases oxygen to drive hydrocarbon oxidation. Reactions were assumed to occur only in the gas phase, based on the observation that reaction rates in the liquid phase are orders of magnitude slower. Therefore, injected hydrogen peroxide first had to vaporize, a process temporally governed by the inter-phase heat and mass transfer rates calculated in the Discrete Phase Model, before participating in any decomposition or combustion reaction. This assumption aligns with similar models reported in literature and supported the use of the Species Transport Model in ANSYS Fluent, which solves individual mass conservation equations for each participating species without relying on stochastic (PDF-based) formulations.

Although the simulation did not explicitly include the catalyst as a separate species, its effect was accounted for indirectly by modifying the Arrhenius reaction rate parameters in the peroxide-kerosene combustion equation. This avoided the need to model catalyst transport or surface chemistry. Instead, catalyst influence was reflected in the lowered activation energy and adjusted pre-exponential factor used in the kinetic rate laws.

Table 3
Reaction mechanism and kinetic parameters.

Reaction Equation	A [s^{-1}]	E_a [kJ/mol]
$H_2O_2 \rightarrow H_2O + 0.5\ O_2$	1.0×10^{13}	75.0
$C_{12}H_{23} + 35.5\ H_2O_2 \rightarrow 12\ CO_2 + 47\ H_2O$	1.0×10^{13}	58.0
$C_{12}H_{23} + 17.75\ O_2 \rightarrow 12\ CO_2 + 11.5\ H_2O$	2.587×10^{9}	125.6

The reaction rate constants were defined using the standard Arrhenius Eq. (5):

$$k = AT^n e^{-E_a/(RT)} \tag{5}$$

where, k is the reaction rate (mol/m^3·s), A is the pre-exponential factor (1/s), E_a is the activation energy (kJ/mol), R is the universal gas constant, T is temperature (K), and n is the global reaction order, assumed to be zero in this study.

The final reaction parameters, compiled in Table 3, were selected based on the best available experimental data, primarily from decomposition studies involving manganese oxide catalysts.

2.4.1. Real gas effects and equation of state

The high pressures and temperatures inside the combustion chamber make the ideal gas law inadequate for describing the behavior of the reacting gases. The combustion products, especially kerosene and its decomposition species, can reach near-supercritical conditions, particularly around the throat and nozzle exit. In these regions, real gas effects have a significant impact on thermodynamic properties such as enthalpy, density, and compressibility. For this reason, the Peng–Robinson real gas model [16] was selected as the equation of state for the simulations. This model is widely used for compressible flow problems involving hydrocarbons and high-pressure systems. It accounts for molecular volume and inter-molecular attraction, offering improved accuracy over the ideal gas model, particularly for kerosene-rich mixtures [17].

In comparative tests, simulations using the Peng–Robinson Real gas model produced more realistic estimates of temperature, density, and flow expansion, reducing the overprediction of nozzle thrust and thermal gradients observed with the ideal gas assumption. Fig. 2 shows the temperature contours for the two gas models. It is clearly visible in the highlighted areas that the real gas model captures the phenomenon far better than its counterpart. These differences were particularly notable in the nozzle where gas expansion accelerates rapidly, and compressibility effects are strongest.

3. Numerical and simulation framework

Building upon the physical system described in the previous section, this part details the numerical strategy used to simulate the thruster's behavior under transient conditions. The framework incorporates unstructured meshing with wall refinement, time-dependent solution schemes, discrete phase modeling for fuel injection, species transport for reaction evolution, and robust turbulence treatment using the *SST k–ω* model. Boundary conditions were defined based on realistic propulsion test environments, while mesh independence and time step sensitivity were thoroughly evaluated to ensure numerical stability and result fidelity.

3.1. Mesh structure and quality

To resolve the complex, unsteady flow and heat transfer within the

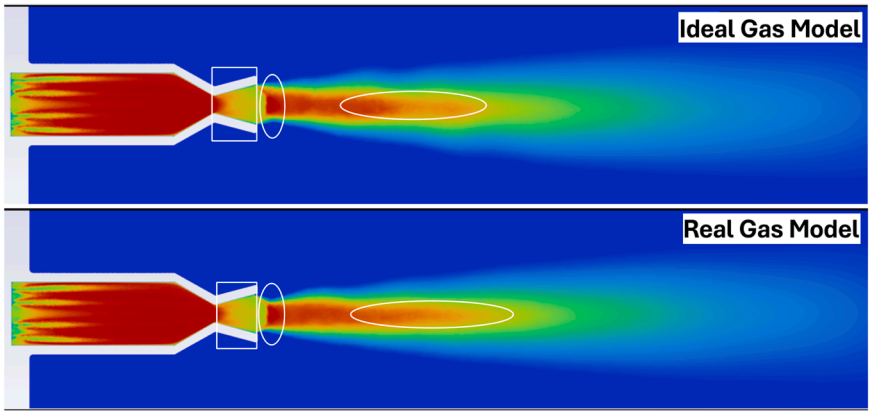

Fig. 2. Comparison of Ideal Gas and Real Gas (Peng-Robinson) models.

Table 4
Mesh resolution parameters.

Mesh	Nodes (Millions)	Elements (Millions)	Injector Face Element Size (mm)	Chamber Element Size (mm)
m2.3x	4.62	15.59	0.50	0.58
m3.7x	5.62	25.31	0.45	0.50
m5.5x	8.37	37.23	0.36	0.40

thruster, a high-quality computational mesh was created using ANSYS Meshing. The aim was to generate a mesh fine enough to capture steep gradients in velocity, temperature, and chemical species concentration, especially near walls, while keeping the overall cell count manageable for transient simulations.

The chamber geometry was discretized using an unstructured tetrahedral mesh due to the complexity of the domain, particularly the nozzle curvature and the cylindrical head-end. This choice allowed flexibility in adapting to the chamber's contours while ensuring smooth cell transitions between regions of different characteristic lengths. Inflation layers were applied at all solid boundaries to accurately resolve the boundary layer, a critical factor in determining wall shear stress and heat flux. A total of ten prism layers were used, with a first-layer thickness of 0.02 mm and a growth rate of 1.2, ensuring adequate near-wall resolution for turbulence modeling using the SST k–ω approach.

To evaluate the sensitivity of results to grid resolution, three mesh configurations were developed: a coarse mesh (m2.3x), a medium-density mesh (m3.7x), and a fine mesh (m5.5x). These were labeled according to their relative refinement levels and total element counts. The detailed mesh resolution parameters of each mesh configuration are given in Table 4. Each mesh preserved geometric fidelity and applied the same boundary condition setup to maintain consistency during comparison.

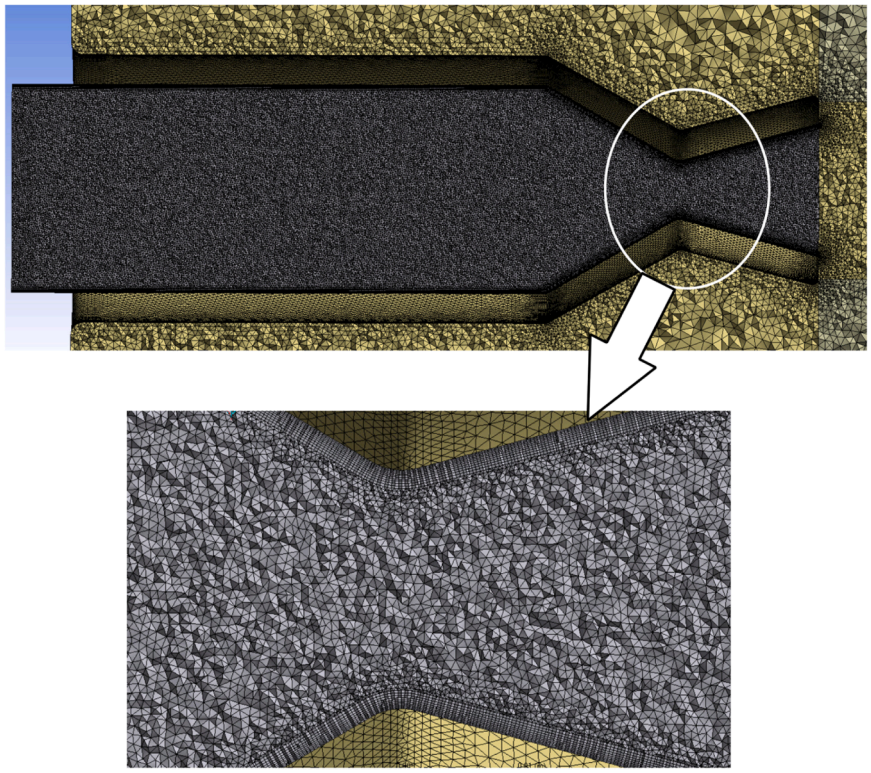

Fig. 3. Final mesh of thruster cross section (top); Nozzle cross section zoomed (bottom).

All mesh versions were evaluated using standard quality metrics. Skewness was maintained below 0.85, the aspect ratio was kept under 4 in all regions, and orthogonality was ensured to remain above 0.20 throughout the domain. These constraints were essential to avoid artificial numerical diffusion and maintain solver stability, particularly in regions of high strain rate and combustion heat release. Although a formal Grid Convergence Index (GCI) calculation was not performed, trends in pressure, temperature, and heat flux converged satisfactorily with mesh refinement, justifying the selection of the fine mesh (m5.5x) as baseline and are presented in section 3.4.

Initial trials with the coarse and medium meshes showed acceptable trends in pressure and temperature, but also revealed minor discrepancies in wall heat flux and nozzle exit velocity. These differences became more pronounced during the early ignition phase, where steep gradients and local hotspots developed rapidly. The fine mesh (m5.5x) demonstrated convergence stability and better agreement with analytical and CEA-predicted values, especially when integrated over time. Although it required longer computational runtimes, it was selected as the baseline for all subsequent simulations because it offered the best balance between resolution and accuracy.

A visual inspection of the mesh revealed that the finest resolution was applied in the combustion chamber core and near the nozzle throat regions where the Mach number transition, thermal gradients, and combustion reactions peaked. By applying local refinement zones, the mesh maintained a uniform y^+ distribution near the wall, ensuring the wall functions of the turbulence model operated within their calibrated range.

The final mesh configuration, as shown in Fig. 3, not only supported accurate prediction of key physical parameters, such as peak flame temperature and thrust, but also provided sufficient resolution to analyze wall heat transfer, stress development, and droplet-gas interactions. This careful meshing strategy, supported by grid independence checks and guided by turbulence modeling constraints, laid a reliable numerical foundation for capturing the full transient behavior of the thruster. With the meshing strategy established and quality metrics verified, it was necessary to ensure that the simulation results themselves were not sensitive to further mesh refinement. A dedicated mesh independence study was therefore conducted, as detailed in Section 3.4.

3.2. Numerical setup and governing equations

3.2.1. Multiphase modeling and flow physics

To simulate the actual behavior of the bipropellant system, a combination of Eulerian and Lagrangian formulations was employed. The oxidizer, high-test hydrogen peroxide (HTP), was treated as a continuous gaseous phase and modeled using the Eulerian approach. Kerosene, which enters the chamber as liquid droplets from the coaxial injector, was modeled as a discrete Lagrangian phase using Fluent's Discrete Phase Model (DPM). This setup allowed the model to resolve interactions between fuel droplets and the gaseous oxidizer, capturing evaporation, heat exchange, and species formation due to combustion.

The governing equations are based on the Reynolds-Averaged Navier-Stokes (RANS) formulation, which, for compressible reactive flow, can be written as Eq. (6):

$$\frac{\partial \boldsymbol{U}}{\partial \boldsymbol{t}} + \nabla \cdot (\boldsymbol{F_c} - \boldsymbol{F_v}) = \boldsymbol{Q} \tag{6}$$

here, U represents the vector of conserved quantities (mass, momentum, energy, and species), F_c and Fv are the convective and viscous fluxes respectively, and Q contains source terms due to combustion heat release and species production.

The Species Transport Eq. (7) describes how the mass fraction of a chemical species changes over time and space within a flowing fluid. It accounts for convection, diffusion, and chemical reactions that either produce or consume the species.

$$\partial(\boldsymbol{\rho Y})/\partial \boldsymbol{t} + \nabla\cdot(\boldsymbol{\rho u Y}) = \nabla\cdot(\boldsymbol{J}) + \boldsymbol{R} + \boldsymbol{S} \tag{7}$$

here, ρ is fluid density (kg/m^3), Y_i is mass fraction of species i, u is velocity vector (m/s), J_i is diffusive flux of species i (kg/m^2·s), R_i is net rate of production of species i due to chemical reactions (kg/m^3·s), and S_i is additional source terms due to droplet evaporation.

In the Lagrangian frame, the motion of each droplet (kerosene, HTP and water) was tracked individually using Newton's second law and represented by Eq. (8) below:

$$\boldsymbol{m_d}\frac{\boldsymbol{dv_d}}{\boldsymbol{dt}} = \boldsymbol{F_D} + \boldsymbol{m_d}\cdot\boldsymbol{g} + \boldsymbol{F_{additional}} \tag{8}$$

where m_d is the droplet mass (kg), v_d its velocity of droplet (m/s), F_D is the drag force on droplet (N), and $F_{additional}$ includes forces such as virtual mass, Saffman lift, and thermophoretic drag. The droplets were injected with a Rosin–Rammler size distribution [18] centered around a mean diameter of 150 μm and a spread parameter of 3.5, consistent with coaxial injector spray characteristics. These values were further validated using the droplet Weber number and injection Reynolds number to ensure physical consistency. Vaporization and heat transfer between droplets and gas were modeled using the infinite conductivity model, assuming thermal equilibrium within each droplet. Furthermore, temperature-dependent latent heat was incorporated to account for the variable energy required for phase change across different temperatures. This two-way coupled Eulerian-Lagrangian system enabled accurate simulation of the transient ignition behavior, capturing the initial propellant breakup, vaporization lag, and its impact on chamber pressure buildup. It also helped reveal the influence of fuel droplet distribution on flame shape and temperature gradients.

3.2.2. Turbulence modeling

To resolve the turbulent nature of the reactive mixing zone and ensure accurate wall heat flux prediction, the Shear Stress Transport (SST) k–ω model was employed. This model is widely used in high-speed combusting flows because of its ability to accurately capture boundary layer effects while transitioning smoothly to k–ε behavior in the free stream.

The governing transport equations for turbulent kinetic energy (k) and specific dissipation rate (ω) are represented by Eqs. (9) and (10) respectively.

$$\frac{\partial(\rho k)}{\partial t} + \nabla\cdot(\rho u k) = \nabla\cdot\left[\left(\mu + \frac{\mu_t}{\sigma_k}\right)\nabla k\right] + P_k - \beta^*\rho\omega \tag{9}$$

$$\frac{\partial(\rho \omega)}{\partial t} + \nabla\cdot(\rho u \omega) = \nabla\cdot\left[\left(\mu + \frac{\mu_t}{\sigma_\omega}\right)\nabla \omega\right] + \alpha\frac{\omega}{k}P_k - \beta\rho\omega^2 \tag{10}$$

where, ρ is the fluid density (kg/m^3), k is the turbulent kinetic energy (m^2/s^2), ω is the specific dissipation rate (1/s), u is the velocity vector (m/s), μ is the molecular dynamic viscosity (Pa·s), μ_t is the turbulent (eddy) viscosity (Pa·s), σ_k is the turbulent Prandtl number for k, σ_ω is the turbulent Prandtl number for ω, P_k is the production of turbulent kinetic energy (kg/m·s^3), and α, β, and β^* are model coefficients specific to the SST k–ω formulation.

To accurately capture the interaction between turbulence and chemistry, the Species Transport model was coupled with the SST k–ω formulation. In this framework, turbulence enhances the mixing of species through the turbulent diffusivity term in the species conservation equations, driven by the turbulent Schmidt number, while the chemical source terms are computed using finite-rate Arrhenius kinetics. This approach assumes that for the hypergolic ignition phase, the reaction rates are kinetically limited rather than mixing limited. Furthermore, the standard turbulence model coefficients were optimized to ensure stability and accuracy in the high-speed compressible regime characteristic of the nozzle expansion, as standard low-speed parameters can lead to excessive dissipation in shock regions.

Table 5
Mesh Statistics and Resolution Details.

Mesh	Element Count	Node Count	Wall Refinement	Inflation Layers	Min. Skewness	Max. Aspect Ratio
m2.3x	~15.5 million	~4.6 million	Yes	Yes	0.20	20
m3.7x	~25.3 million	~5.6 million	Yes	Yes	0.20	20
m5.5x	~37.2 million	~8.4 million	Yes	Yes	0.20	20

The SST model's near-wall accuracy made it well-suited for capturing the steep thermal gradients and skin friction in the combustion chamber and throat regions. Large Eddy Simulation (LES), although potentially more accurate for transient ignition phenomena, was not feasible due to prohibitive computational costs associated with resolving fine-scale turbulence throughout the entire combustion domain. Turbulent mixing between the fuel and oxidizer was crucial for flame anchoring and heat release rate stabilization. A turbulent Prandtl number of 0.85 was used, and scalable wall functions were applied in regions where y^+ values permitted. In high-temperature regions, especially near the throat and exit, the turbulence model played a key role in predicting entrainment of hot gases and expansion-induced instabilities.

3.2.3. Solver setting

The simulation used a pressure-based implicit solver to handle the compressibility effects associated with rapid pressure changes and sonic-to-supersonic flow transition in the nozzle. Time stepping was performed using a fully implicit scheme, with time steps automatically refined based on Courant number and local residual behavior. Radiation heat transfer was neglected in this study. Given the short combustion chamber length, relatively low optical thickness of the reacting gases, and dominant convective and conductive heat transfer modes, radiative effects were expected to have a minimal impact on thermal loads. During the ignition phase, time steps as small as 1×10^{-7} s were used, while in quasi-steady phases they increased to 5×10^{-5} s.

The solution was initialized using patched values to represent ambient temperature (288.15 K) and pressure (1 atm), while a small pre-ignition temperature (300 K) was applied at the oxidizer inlet to simulate catalyst-induced peroxide decomposition. All simulations were run for 70 ms, corresponding to an estimated ignition and stabilization period typical for this scale of thruster.

Residuals were monitored for all variables, and convergence at each time step was ensured by reducing energy and species residuals below 1×10^{-6}. It is noted that this study employs a deterministic CFD approach; therefore, the results presented for each propellant configuration represent single numerical realizations under fixed initial and boundary conditions, without stochastic variation. Additional monitors tracked pressure at the chamber head, nozzle exit velocity, and wall temperature rise to ensure physical fidelity and numerical convergence throughout the simulation.

3.3. Boundary conditions

A physically realistic boundary condition setup was critical to simulate startup behavior, avoid artificial reflections, and ensure that combustion developed naturally from the inlet conditions. Both fuel and oxidizer were injected at 300 K, with a total pressure of 15 bar, twice the target chamber pressure, to account for pressure drop across the injector. Because the injector plate was omitted in the geometry, droplets were introduced directly via discrete phase injection on the inlet face using experimentally validated spray characteristics. The inlets were defined as mass flow inlets with zero continuous flow rate but assigned the appropriate gauge pressure and droplet parameters. The outlet was modeled as a pressure outlet at sea-level conditions (101,325 Pa, 288.15 K). Gravity was included as a body force acting perpendicular to the flow axis, with $g = 9.81$ m/s^2. Reverse flow was allowed to accommodate transient oscillations during ignition. Farfield boundaries were extended 15–20 times the chamber length (2520 mm) to suppress artificial reflections. Wall treatment was particularly important for accurate temperature prediction. A variety of wall boundary treatments were tested, including adiabatic wall assumption (no heat loss), constant wall temperatures of 300 K and 1800 K, and polynomial wall temperature profile fitted from a steady-state thermal analysis. These cases were compared using pressure, velocity, and temperature contours. Ultimately, the adiabatic assumption was selected due to its numerical stability and the minimal deviation ($\leq$2 %) observed in key flow variables across cases. While this slightly overpredicts chamber temperature, it avoids artificially injecting or removing energy during the early ignition phase, which would distort the transient behavior.

3.4. Mesh independence validation

While Section 3.1 detailed the generation and structural quality of the computational mesh, this section focuses on validating the independence of simulation results from mesh resolution by systematically refining the grid and analyzing key performance indicators. To ensure the reliability and spatial resolution of the computational model, a mesh independence study was conducted. This section aimed to determine whether further refinement of the mesh would produce any significant improvement in the accuracy of simulation results. The standard parameters were compared across meshes of increasing resolution while keeping consistent boundary conditions and solver settings.

3.4.1. Mesh design and configuration

Three mesh configurations were used for this study: m2.3x, m3.7x, and m5.5x. These were derived by uniformly refining or coarsening the mesh sizing parameters relative to a reference mesh (m1.0x), then applying targeted wall refinement and inflation layers. All meshes were generated using tetrahedral elements to preserve geometric conformity across the combustion chamber and nozzle. Transition regions and boundary layers were treated carefully using inflation layers to resolve steep gradients in temperature and velocity near the chamber walls. Element quality was improved through ICEM-based cleanup, ensuring minimum skewness and orthogonal quality values above recommended thresholds.

Each simulation was run for a total of 20-time steps of 1 ms each. The final step was extended to 500 iterations to evaluate residual convergence. All cases were run on a 40-core system with 160 GB RAM to ensure consistency in runtime performance and hardware utilization.

The data presented in Table 5 indicate that as the mesh resolution increases from m2.3x to m5.5x, there is a significant increase in the total number of elements and nodes. Specifically, the fine mesh (m5.5x) has more than double the number of elements compared to the coarse mesh (m2.3x). Despite the refinement, the minimum skewness and maximum aspect ratio were successfully maintained within recommended quality thresholds across all mesh levels, demonstrating that higher mesh resolution was achieved without compromising numerical stability. The consistent application of wall refinements and inflation layers in all cases ensures that critical near-wall physics, such as boundary layer formation and wall heat transfer, are captured with high fidelity regardless of the global mesh density.

3.4.2. Mesh influence on simulation output

As mesh resolution increased, noticeable improvements were

Table 6
Mesh Independence Results.

Mesh Size	Max Temp (K)	Max Pressure (bar)	Max Velocity (m/s)	Thrust (N)	Runtime (hrs)
m2.3x	3214.12	7.34	2345	59.38	5.21
m3.7x	3274.79	7.64	2378.16	62.86	8.13
m5.5x	3274.83	7.67	2400.38	63.22	12.66

observed in thrust prediction, chamber pressure accuracy, and flow feature definition. The finer meshes produced better resolution of shear layers, nozzle shock patterns, and flame anchoring behavior. However, the incremental gain in key output variables diminished as the mesh size approached m5.5x.

Table 6 summarizes the mesh independence study results, showing maximum temperature, pressure, velocity, thrust, and runtime across different mesh sizes. Notably, thrust improved significantly from 59.38 N at m2.3x to 63.22 N at m5.5x, while runtime also increased substantially, highlighting the trade-off between accuracy and computational cost.

This trend is visualized in Fig. 4, where maximum temperature, pressure, velocity, and thrust are plotted as bar charts (logarithmic values) across the different mesh sizes, accompanied by a line plot representing runtime. The figure clearly shows that as the mesh is refined, improvements in physical quantities (such as thrust and velocity) plateau, whereas the computational cost (runtime) continues to rise steeply. Particularly, the jump in runtime from 8.13 hours for m3.7x to 12.66 hours for m5.5x emphasizes the diminishing returns in simulation accuracy relative to computational expense.

Further analysis in Table 7 quantifies the maximum deviation between medium (m3.7x) and fine (m5.5x) meshes across critical physical parameters. The deviation in thrust was 0.57 %, while pressure and velocity varied by 0.30 % and 0.93 %, respectively. Temperature deviation was effectively zero (0.000012 %), confirming that thermal predictions had fully converged.

Fig. 5 presents a detailed comparison between medium and fine mesh configurations by plotting the maximum velocity, pressure, temperature, and thrust values side-by-side. For each parameter, the graphs include annotations showing the calculated percentage deviation between meshes. These plots demonstrate that although there is a slight increase in each value with finer mesh, the relative difference remains below 1 % for all key parameters, further confirming mesh independence. The small variations illustrated in Fig. 5 validate that the m3.7x mesh already achieves sufficient accuracy and moving to m5.5x provides only marginal improvements at much higher computational cost.

3.4.3. *Effect of time step size on mesh behavior*

In addition to spatial resolution, the effect of temporal discretization on simulation stability and accuracy was examined. As shown in Fig. 6, thrust curves generated with different time step sizes and mesh configurations indicated that finer meshes require more time to reach steady-state behavior. Simulations using the m5.5x mesh with a smaller time step of 0.5 ms demonstrated a faster rise in thrust compared to simulations run with the default 1 ms step. Both configurations ultimately converged to the same final thrust value, but the transient behavior, specifically the rate of thrust buildup, was clearly influenced by the time-stepping approach. This is attributed to the solver's relaxation factor settings, which limit the rate at which variables such as pressure are updated between iterations. For instance, with a pressure relaxation factor of 0.3, only 30 % of the computed pressure change is applied per iteration. Thus, while the result remains consistent, a smaller time step compresses more physical change into each second of simulation time and requires more iterations to fully resolve.

These observations suggest that while finer meshes offer better accuracy, they must be accompanied by appropriate time step tuning and increased iteration counts to capture transient dynamics effectively. Since the CFD model uses finite-rate chemistry with uncertain reaction parameters, the simulation's ability to resolve short-timescale behavior is inherently limited. As a result, the emphasis was placed on matching final performance indicators (thrust, chamber pressure) rather than attempting to resolve transient ignition details, which were not available experimentally for validation.

Table 7
Maximum parameter deviation between medium (m3.7x) and fine (m5.5x) mesh configurations.

Parameter	Medium (m3.7x)	Fine (m5.5x)	Deviation (%)
Velocity [m/s]	2378.16	2400.38	0.93 %
Pressure [10^5 Pa]	7.64	7.67	0.30 %
Temperature [K]	3274.79	3274.83	0.00 %
Thrust [N]	62.86	63.22	0.57 %

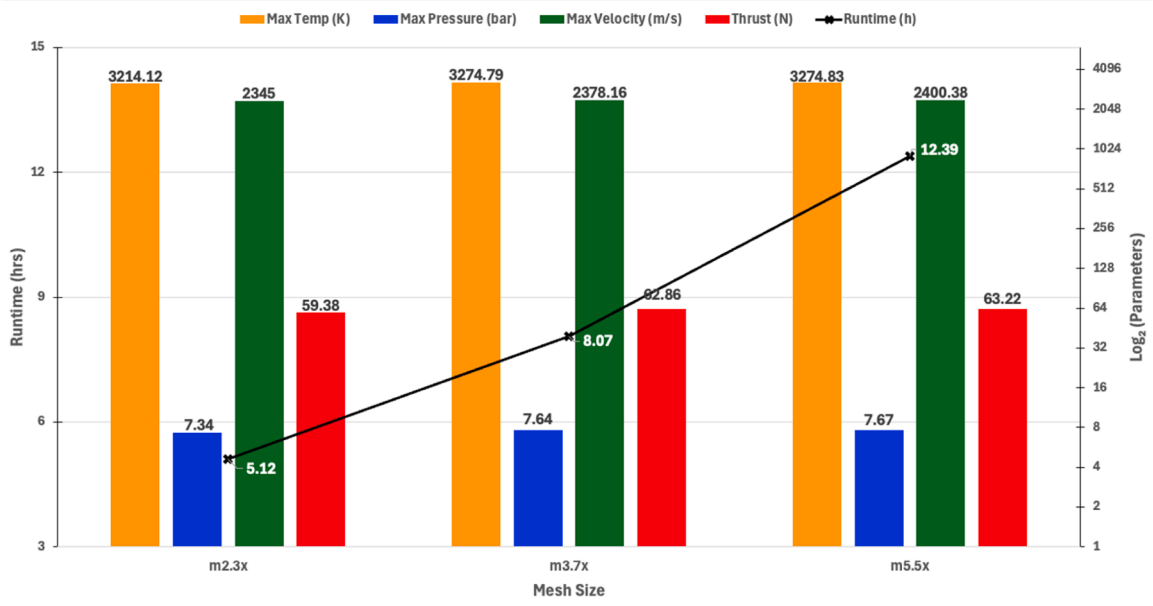

Fig. 4. Variation of key output parameters and runtime with mesh refinement.

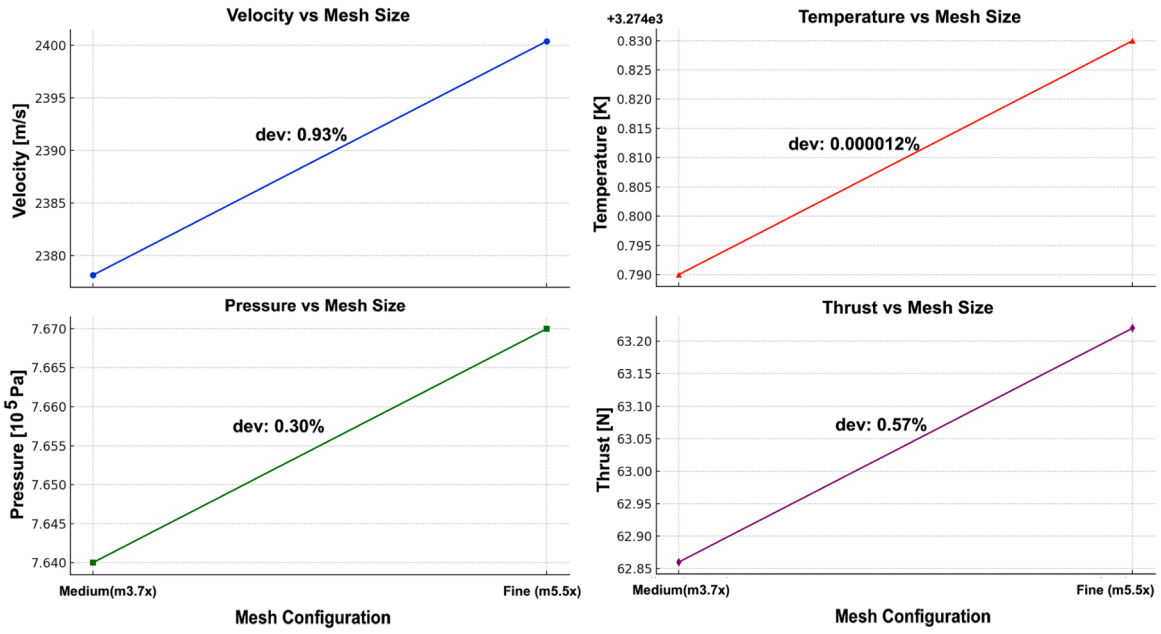

Fig. 5. Deviation analysis between medium (m3.7x) and fine (m5.5x) meshes for major physical quantities.

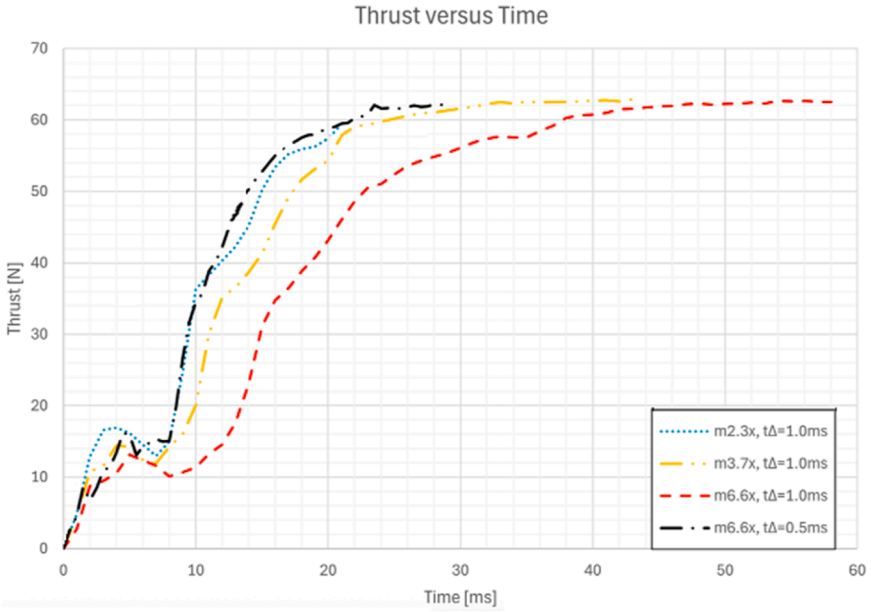

Fig. 6. Thrust versus Time for different meshes and time-step sizes.

4. Results and discussion

This section presents the simulation results and interprets the key physical parameters that define engine performance, internal flow dynamics, and structural loading on the combustion chamber. These analyses follow the framework outlined in the previous sections (2–3) and are based on the four propellant combinations investigated during this study. While global performance metrics are presented first, specific attention is drawn to the exhaust species analysis in Section 4.3, which explains the causes of performance deviations, most notably the significant unburnt fuel fractions observed in fuel-rich mixtures. As previously discussed in Section 2.3, the two oxidizer concentrations selected were

Table 8
Overview of the simulations performed.

Injector Type	H_2O_2 Concentration (α)	Equivalence Ratio (Φ)	O/F Ratio	$I_{sp,vac}$ [s]	$\dot{m}$ [10^{-3} kg/s]	Identifier
Coaxial	98 %	1.00	7.39	277.4	36.75	c98st
	98 %	1.15	6.42	279.4	36.50	c98hp
	95 %	1.00	7.62	274.7	37.12	c95st
	95 %	1.10	6.93	276.3	36.89	c95hp

Table 9
Thrust for different propellants and deviation from the default case (α = 98 %, Φ = 1.00).

Case	Thrust [N]	Relative Difference
α = 98 %, Φ = 1.00	63.22	—
α = 98 %, Φ = 1.15	61.88	−2.11 %
α = 95 %, Φ = 1.00	63.00	−0.34 %
α = 95 %, Φ = 1.10	62.09	−1.78 %

98 % and 95 % HTP. For each concentration, both a stoichiometric mixture and a slightly fuel-rich mixture, identified as the highest-performing combination from NASA CEA results, were evaluated (Fig. 1). The specific conditions used for each simulation, including equivalence ratio, O/F ratio, vacuum specific impulse, and total mass flow rate, are summarized in Table 8.

To study the transient behavior of the engine, key flow variables such as temperature, pressure, and velocity were monitored at each time step. These parameters were analyzed in detail for the baseline configuration using 98 % HTP at stoichiometric conditions (*c98st*), and representative contour snapshots were extracted to illustrate their spatial and temporal evolution. It is important to note that all results are specific to the selected Arrhenius parameters used in the reaction modeling. While the trends and magnitudes observed are physically meaningful, a change in catalyst composition or activation energy could shift the timing of ignition and flame development, though the overall behavior would likely remain qualitatively similar.

4.1. Engine performance

The engine performance was evaluated across four different propellant configurations, combining two concentrations of hydrogen peroxide (α = 95 % and 98 %) with stoichiometric and fuel-rich equivalence ratios. The objective was to maintain a constant vacuum thrust of 100 N across all cases while studying how these variations affect performance metrics such as thrust, specific impulse, and mass flow rate. Since the theoretical specific impulse (I_{sp}) varies with propellant concentration and mixture ratio, as determined by CEA simulations, the mass flow rate was adjusted for each case to maintain the target thrust. This ensured that the combustion efficiency and loading conditions could be meaningfully compared across configurations, without the confounding influence of differing thrust levels.

Table 9 summarizes the resulting thrust values from the simulations and their deviations from the reference case (α = 98 %, Φ = 1.00). While all setups were tuned to achieve the same vacuum thrust, slight differences remained in the sea-level equivalent thrust due to variations in chamber pressure and the combustion behavior. Among the stoichiometric cases, the 98 % HTP mixture produced the highest thrust, with the 95 % stoichiometric mixture following closely. Both outperformed their fuel-rich counterparts, indicating that fuel-rich combustion, although theoretically yielding higher I_{sp}, does not necessarily translate into higher practical thrust when real flow and reaction dynamics are considered.

These results suggest that while small, the performance difference between propellant combinations is not negligible and can influence design decisions, especially when structural loads, material temperature limits, and chamber sizing are also considered. Interestingly, all simulated thrust values were found to be higher than the analytical sea-level thrust estimate of 60.04 N. This discrepancy likely stems from slight increases in chamber pressure in the simulations and the combustion behavior modeled through finite-rate chemistry rather than equilibrium-based assumptions.

The transient thrust behavior over the 50 ms simulation period is shown in Fig. 7. All configurations exhibited similar trends, a rapid increase in thrust during the first few milliseconds, followed by a temporary decline between 5 ms and 8 ms, and a final rise as the flow stabilized. The temporary drop in thrust corresponds to a period of flow separation within the nozzle, as identified in the velocity contours, where the combustion gases began to detach from the nozzle wall. This separation reduces the effectiveness of nozzle expansion, temporarily decreasing thrust. As the flow field developed and pressure equilibrated, reattachment occurred and thrust resumed its upward trend. A true steady state was reached around 50 ms, where the thrust values flattened and no longer changed significantly with time.

The differences in required mass flow rates to maintain 100 N vacuum thrust are shown in Fig. 8, comparing both CEA-based predictions (orange line) and simulation-derived values (blue line). As expected from chemical equilibrium theory, higher HTP concentrations and equivalence ratios produce higher specific impulses (according to CEA), leading to reduced required mass flow rates. However, the CFD results show a slight deviation from this trend: while higher peroxide concentration still improves performance, the stoichiometric mixtures perform better than the fuel-rich ones, contrary to the ideal prediction. This deviation is attributed to the impact of combustion inefficiencies, increased thermal loading, and potentially slower reaction rates in fuel-rich configurations, factors that are not captured in the CEA equilibrium model. In practice, a fuel-rich mixture may suffer from incomplete combustion or localized quenching, especially near the chamber walls, which reduces thrust efficiency.

Fig. 8 also illustrates that, from a purely mass optimization

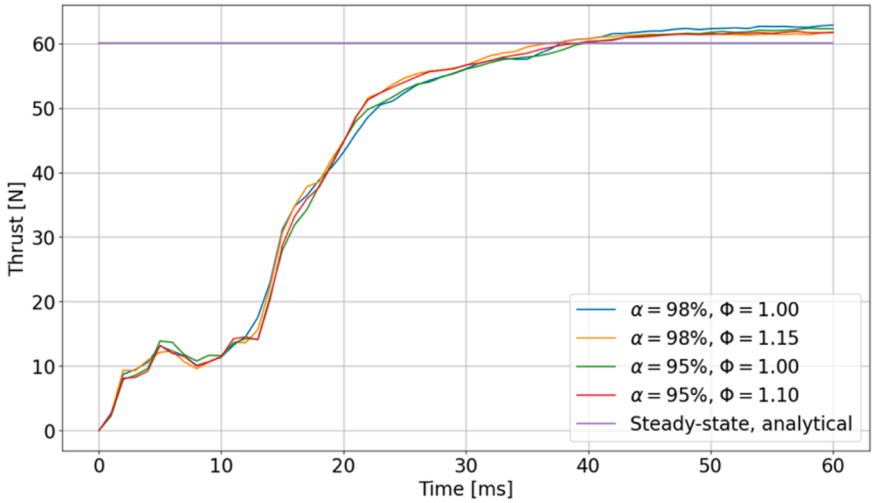

Fig. 7. Thrust over time for different propellants compared to the analytical value based on CEA data.

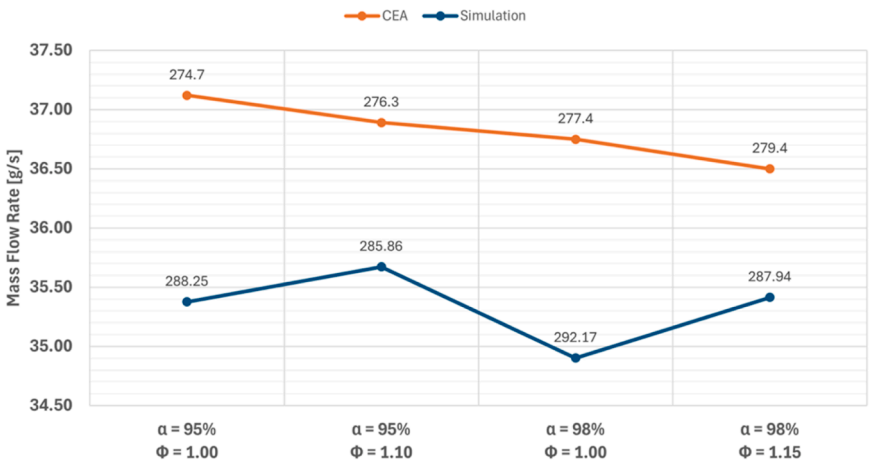

Fig. 8. Mass Flow Rate to obtain a Vacuum Thrust of F = 100 N for Varying Propellants, according to CEA and derived from simulations; I_{sp} [s] is given for each fuel combination.

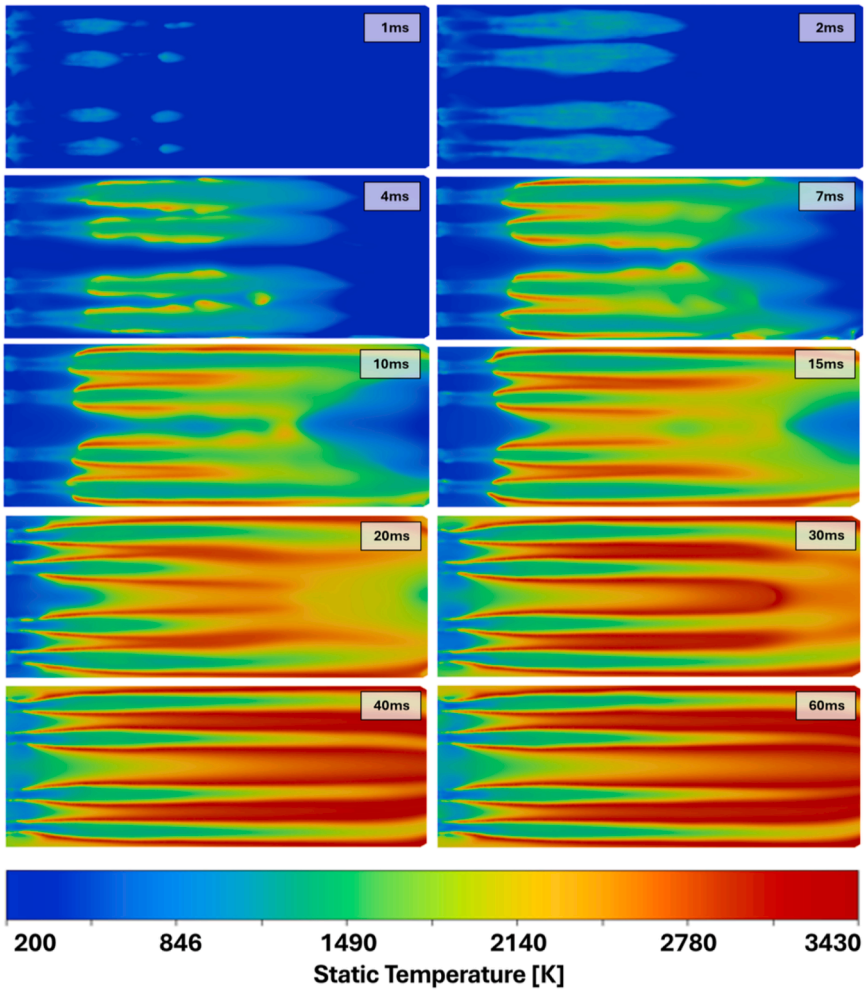

Fig. 9. Static chamber temperature over time (Injector to Nozzle Entrance).

perspective, CEA would recommend operating at α = 98 % and Φ = 1.15, as this yields the highest I_{sp} and the lowest required mass flow. However, the CFD results suggest that α = 98 % with Φ = 1.00 actually delivers better performance under real, transient conditions. This discrepancy underscores the importance of using high-fidelity simulations when evaluating propellant combinations, as they reveal subtle but critical interactions that simple thermochemical models might overlook. The maximum variation in mass flow rate across all tested cases was approximately 2 %, which appears minor but may become significant when considered alongside structural stresses and thermal limits. For instance, a higher mass flow rate leads to higher total energy input into the chamber, which could intensify wall heating and mechanical

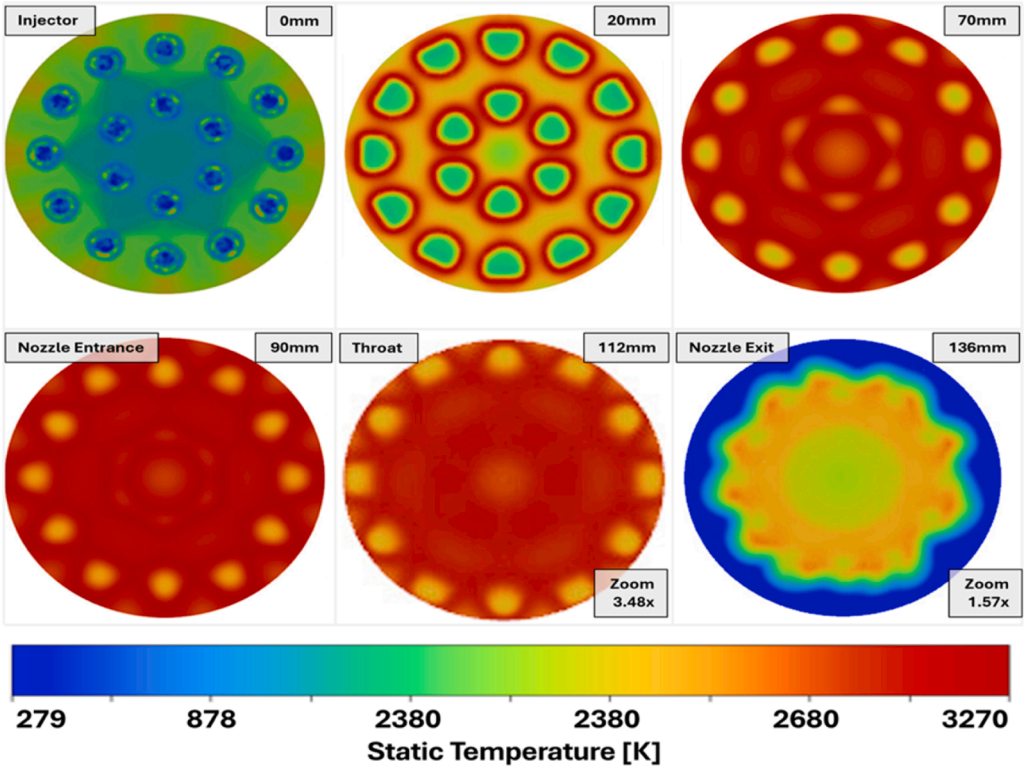

Fig. 10. Change in temperature throughout the chamber (steady state, α = 98 %, Φ = 1.00); throat and nozzle exit are enlarged.

loading. Therefore, even small differences in flow rate must be evaluated in the broader context of thermal-structural coupling and system-level constraints.

4.2. *Internal flow field evolution*

To understand the internal behavior of the thruster, the flow evolution was studied in terms of static temperature, absolute pressure, and velocity magnitude across time and along the engine axis. The goal of this analysis was to track the development of the combustion process, identify transient features like ignition and shock structures, and assess the impact of different propellant combinations on core flow properties. The simulations revealed how the combustion process propagates within the chamber, how shocks form and evolve in the nozzle, and how these dynamics influence performance indicators such as pressure distribution and exhaust velocity. The results in this section are based on high-resolution visualizations and data extracted from the simulation domain, with the *c98st* case (α = 98 %, Φ = 1.00) used as the reference configuration.

4.2.1. *Static temperature*

4.2.1.1. Transient development of temperature. Combustion activity began rapidly, with reaction zones forming within the first millisecond of simulation time. As shown in Fig. 9, four distinct high-temperature regions appeared near the oxidizer inlets, corresponding to the four oxidizer jets intersecting the cross-sectional plane. These early zones of elevated temperature were primarily due to the thermal decomposition of hydrogen peroxide, which was the dominant reaction during initial time steps. Despite its higher activation energy, the decomposition reaction did not require the presence of fuel and could proceed independently within the oxidizer stream, explaining its early onset and dominance, found to be roughly three orders of magnitude more frequent than combustion reactions based on reaction rate analysis.

Over the next few milliseconds, these decomposition zones expanded downstream, and ignition occurred around t = 7 ms, marked by a sharp increase in local temperature. As combustion spread, the high-temperature regions extended both toward the nozzle and backward toward the injector face. Notably, temperature near the chamber wall rose more rapidly than at the centerline, owing to the injector layout that placed many oxidizer jets close to the wall, promoting intense mixing and reaction in those regions. By t = 40 ms, the chamber was nearly fully developed thermally, though some colder regions near the injector base remained. By t = 60 ms, combustion zones had narrowed slightly, and the four coaxial injection elements remained clearly visible in cross-section. In the nozzle, the temperature increase was first observed around t = 10 ms. Temperature at the nozzle wall rose before the center, an indication that the wall-bounded combustion was particularly active during the early expansion phase. As the flow exited the chamber (t = 20 ms), flow separation occurred in the nozzle's divergent section due to overexpansion under sea-level backpressure. This led to the formation of shock diamonds by t = 30 ms, a typical pattern resulting from alternating compression and expansion waves downstream of the throat.

4.2.1.2. Spatial variation and fuel effects. Temperature distribution at 60 ms along the symmetry axis is shown in Fig. 10, highlighting key features of the flow. The region immediately downstream of the oxidizer injector remained cooler, with decomposition zones around 1350 K, closely matching the 1394 K value predicted by CEA for 98 % HTP. At x = 0.02 m, red-colored zones denoting active combustion appear at the interface between the oxidizer and kerosene, confirming that mixing-driven ignition occurred at the boundary of these two streams. Due to the location of 12 out of 18 injectors near the wall, much of the combustion energy was released in near-wall regions, explaining the asymmetric temperature build-up.

The axial temperature profiles for all four propellant cases are presented in Fig. 11. Near the injector, temperatures remained low in all cases due to limited combustion activity. Temperatures increased rapidly downstream, reaching a peak just before the throat at $x \approx 0.11$

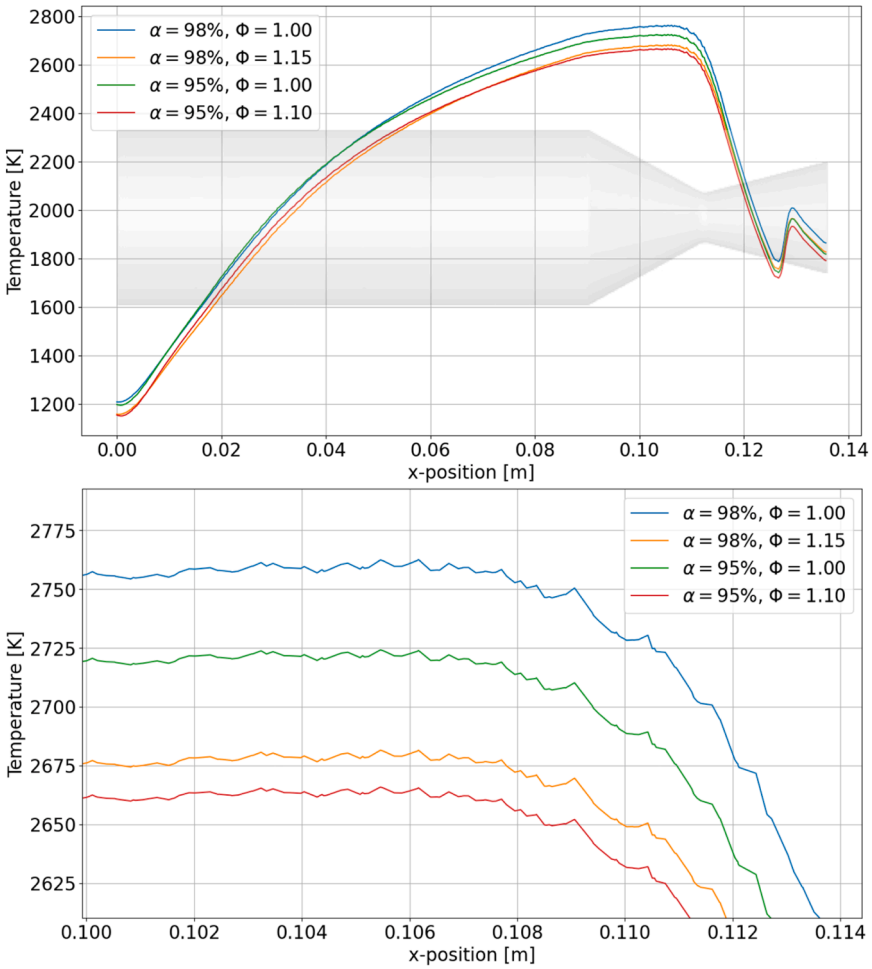

Fig. 11. Static Temperature along the chamber symmetry axis for different propellants; whole chamber (top) and zoomed near throat (bottom).

m, as combustion reached maximum intensity. Downstream of the throat, a sharp drop in temperature was observed due to rapid expansion, followed by localized peaks corresponding to shock compression zones. The irregularity in these plots, especially near the throat, is attributed to mesh-related interpolation effects along the centerline in an unstructured grid, where steep radial gradients make values sensitive to exact sampling locations.

When the maximum axial temperatures obtained from simulations were compared against the CEA predictions it was found that the stoichiometric cases deviated less than 1 % from equilibrium estimates, while fuel-rich cases showed deviations within 5 %. Interestingly, contrary to CEA's expectations, the fuel-rich mixtures resulted in lower temperatures than stoichiometric ones. This is likely due to incomplete combustion or fuel dilution effects, where excess kerosene absorbs energy but does not fully react, an effect that is explored further in section 4.3.

4.2.2. *Absolute pressure*

The pressure field followed a predictable pattern for a supersonic nozzle under sea-level conditions. The pressure within the chamber was relatively uniform during early time steps and dropped sharply across the throat. As the combustion intensified, pressure rose rapidly, reaching over 90 % of the final steady-state value by t = 30 ms. From t = 40 ms onward, chamber pressure remained nearly constant, indicating the onset of a quasi-steady condition. Meanwhile, the nozzle flow continued to evolve, as evidenced by changes in the downstream shock structure. As shown in Fig. 12, pressure profiles along the chamber axis were broadly similar across all propellant combinations.

Peak pressures ranged from 7.54 bar (fuel-rich 98 %) to 7.66 bar (stoichiometric 98 %), which is within a 1.24 % spread and deviates from the CEA reference pressure of 7.50 bar by no more than 2.18 %. These small differences are attributed to varying degrees of combustion completeness and local reaction intensity. As with temperature, pressure dropped significantly across the throat ($x \approx 0.11$ m) and underwent minor increases due to shock formation and recompression effects downstream.

4.2.3. *Velocity magnitude*

The flow velocity began to increase immediately following ignition. By t = 2 ms, a high-velocity zone had formed near the throat, propagating downstream over time. By t = 10 ms, the onset of an oblique shock and corresponding flow separation could be observed. These features intensified by t = 22 ms, with the formation of additional shocks and expansion fans in the nozzle's divergent section. From t = 30 ms to 60 ms, the general structure remained unchanged, but the features expanded axially as the flow matured. Velocity contours, as shown in Fig. 13, closely followed the high-temperature zones during the early phase ($t \leq 7$ ms), after which velocity was dominated by nozzle dynamics.

The impact of propellant composition on velocity is illustrated in Fig. 14. Up to the throat, velocity remained nearly identical for all configurations, consistent with the fact that upstream of the throat, subsonic flow is governed by chamber pressure and geometry. Beyond the throat, velocity increased rapidly as the flow expanded. The peak velocity occurred in the nozzle divergent section before flow separation at $x \approx 0.1265$ m. The maximum velocity ranged from 2212 m/s (*c98hp*)

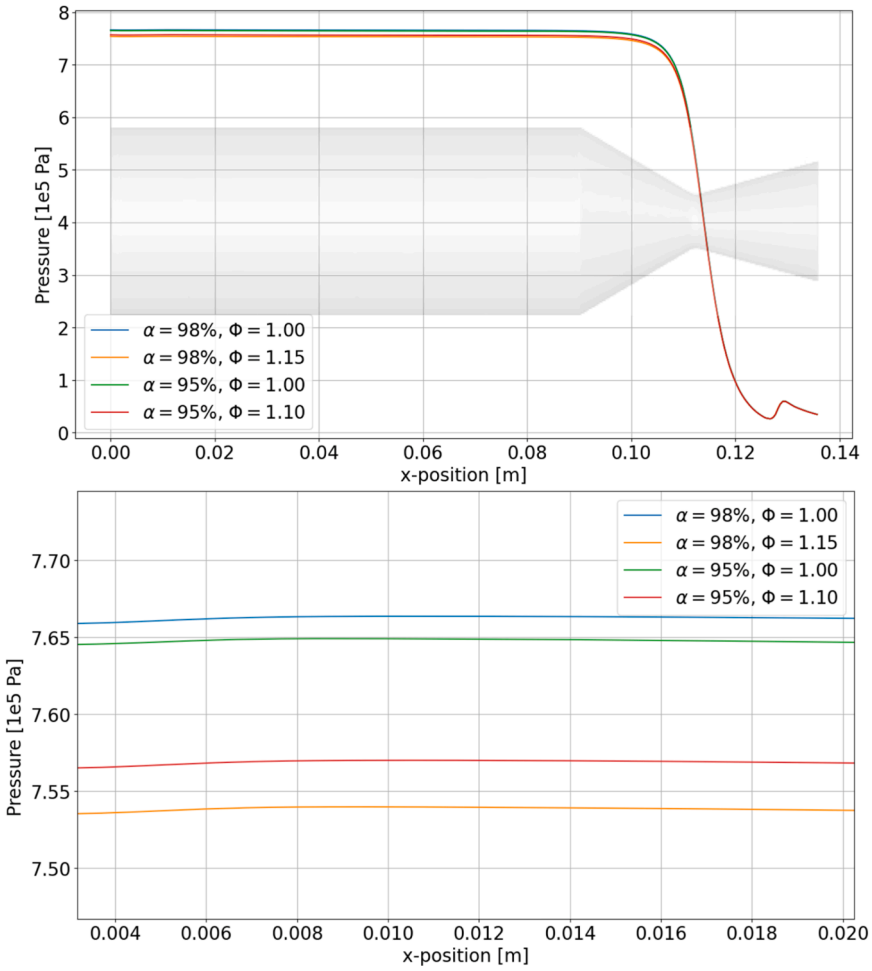

Fig. 12. Absolute Static Pressure along the chamber symmetry axis for different propellants; whole chamber (top) and zoomed near injector (bottom).

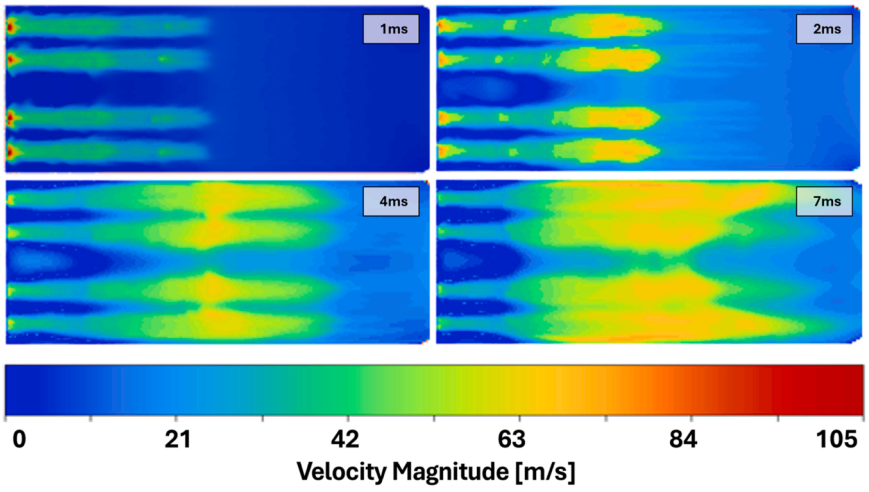

Fig. 13. Chamber Velocity magnitude contour over Time.

to 2261 m/s (*c98st*), showing that stoichiometric mixtures resulted in slightly higher exit velocities, conforming with the earlier observation that they also produced higher combustion temperatures and pressures.

4.3. Combustion product composition and emissions

The composition of exhaust gases was analyzed to better understand the differences observed in thrust and combustion temperature across various propellant combinations. Since the simulations showed notable performance deviations between stoichiometric and fuel-rich cases, particularly in thrust (4.1) and chamber temperature (4.2.1), an evaluation of species distribution at the throat and nozzle exit was carried out to investigate the degree of combustion completeness and identify the presence of unburnt reactants.

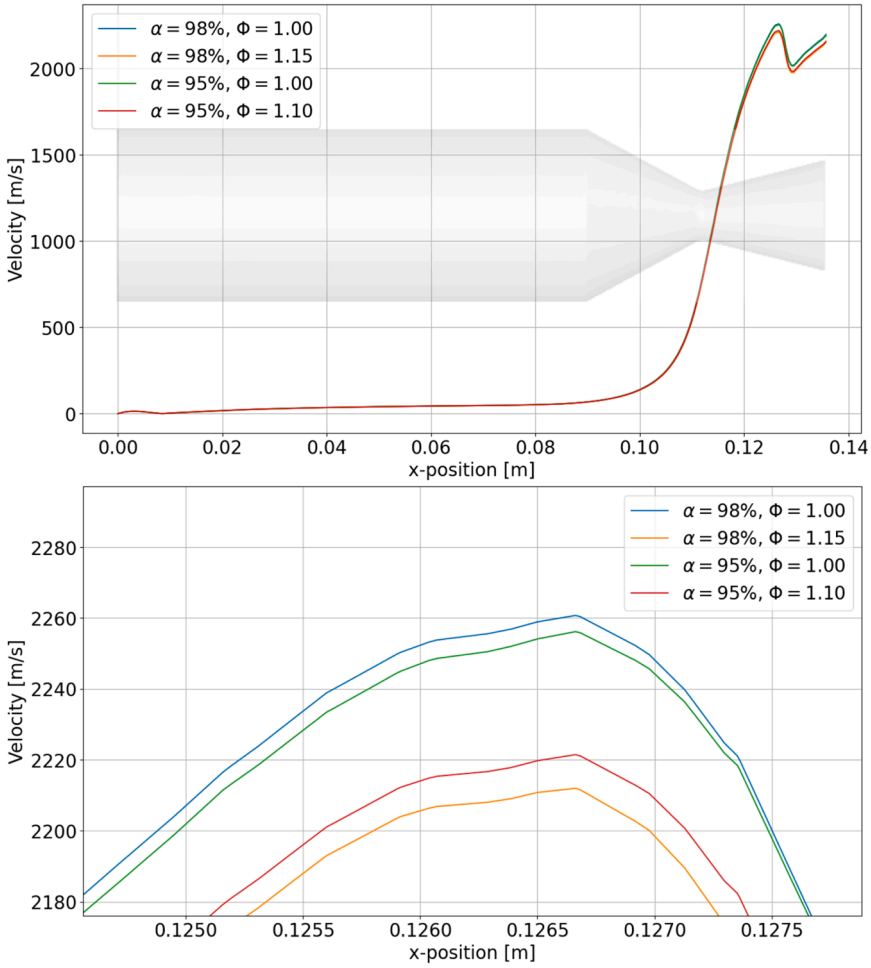

Fig. 14. Velocity Magnitude along the chamber symmetry axis for different propellants; whole chamber (top) and zoomed at separation point (bottom).

Table 10
Peak kerosene concentration for different cases; relative values are given for fuel-rich cases with respect to the corresponding stoichiometric case.

Case	$c_{(C_{12}H_{23})}$ (Throat)	$c_{(C_{12}H_{23})}$ (Exit)
α = 98 %, Φ = 1.00	6.47	5.67
α = 98 %, Φ = 1.15	7.84 (+21.20 %)	7.10 (+25.29 %)
α = 95 %, Φ = 1.00	5.77	5.02
α = 95 %, Φ = 1.10	6.68 (+15.66 %)	6.01 (+19.65 %)

4.3.1. *Unburnt fuel and mixing effects*

A clear trend of fuel-rich cases exhibiting significantly higher mass fractions of unburnt kerosene at both the throat and nozzle exit is observed. As shown in Table 10, the relative increase in kerosene mass fraction for the fuel-rich mixtures was greater than the corresponding increase in fuel injected, indicating inefficient combustion. For instance, in the case of α = 98 %, Φ = 1.15, the injected fuel was 15 % higher than its stoichiometric counterpart, but the unburnt fuel at the nozzle exit was more than 25 % higher suggesting that the additional kerosene was largely vaporized but not combusted.

These patterns were further visualized in Fig. 15, which shows kerosene concentration profiles aligned with the coaxial injector layout. High local concentrations of fuel persisted in the chamber centerline and between injection elements, while oxidizer-rich zones remained closer to the walls. This spatial mismatch highlights an underlying issue with poor propellant mixing, where oxidizer and fuel do not overlap sufficiently for complete reaction, particularly in the fuel-rich scenarios. The result is incomplete combustion, reduced heat release, and ultimately lower thrust and flame temperature.

4.3.2. *Mass fraction analysis at nozzle exit*

The species mass fractions at the nozzle exit, averaged over the full area using mass-weighted integration, are summarized in Table 11. Water vapor and carbon dioxide dominated the exhaust in all cases, as expected. Notably, the amount of unburnt kerosene in the exhaust stream more than doubled in fuel-rich mixtures compared to stoichiometric ones, reaching up to 1.80 % by mass in the most fuel-rich case (*c98hp*). The presence of oxygen in the exhaust despite excess fuel indicates that incomplete combustion was not due to oxidizer shortage, but rather to localized poor mixing.

4.3.3. *Atmospheric backflow and oxygen consumption*

Due to flow separation in the nozzle under sea-level backpressure, the simulation predicted that atmospheric gases, modeled as 21 % oxygen and 79 % nitrogen, entered the nozzle from downstream. To isolate the engine's contribution to oxygen levels, the mass fraction of atmospheric oxygen was subtracted, and the exhaust composition was scaled accordingly. Table 12 shows this correction for different cases undertaken in the simulations. In the case of *c98hp*, the corrected oxygen mass fraction turned negative, indicating that the model predicts the combustion process had continued past the nozzle exit and even consumed atmospheric oxygen, suggesting persistent unburnt fuel and post-combustion mixing. While negative value has no physical meaning per se, they signal that more oxygen was consumed than supplied by the engine's oxidizer stream alone.

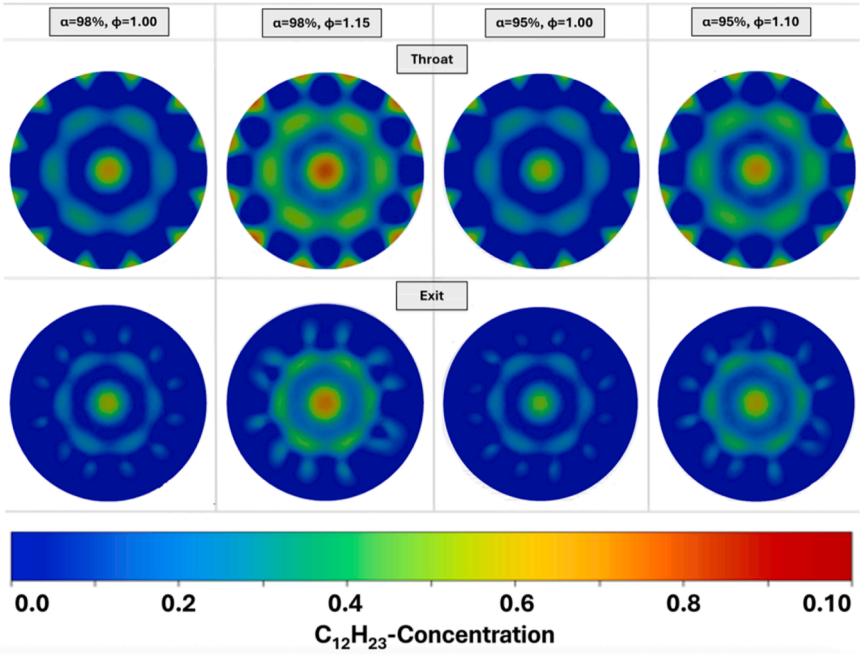

Fig. 15. Kerosene mass concentration at throat (top) and nozzle exit (bottom) for different propellants.

Table 11
Total Species composition by mass at Nozzle exit.

Case	$C_{12}H_{23}$	H_2O	O_2	CO_2	N_2
c98st	0.81 %	45.09 %	6.40 %	26.40 %	21.31 %
c98hp	1.80 %	44.45 %	5.43 %	26.75 %	21.57 %
c95st	0.76 %	45.78 %	6.44 %	25.58 %	21.44 %
c95hp	1.40 %	45.44 %	5.74 %	25.92 %	21.51 %

Table 12
Mass fraction correction for atmospheric backflow.

	c98st	c98hp	c95st	c95hp
Atmosphere	26.97 %	27.30 %	27.14 %	27.23 %
Exhaust	73.03 %	72.70 %	72.86 %	72.77 %
O_2 corrected	0.74 %	-0.30 %	0.74 %	0.02 %

Table 13
Exhaust species composition by mass at Nozzle exit.

Case	$C_{12}H_{23}$	H_2O	O_2	CO_2	Unburnt Fuel (%)
c98st	1.10 %	61.74 %	1.01 %	36.14 %	8.80 %
c98hp	2.48 %	61.14 %	−0.42 %	36.80 %	17.58 %
c95st	1.04 %	62.83 %	1.02 %	35.11 %	8.56 %
c95hp	1.92 %	62.44 %	0.03 %	35.62 %	14.56 %

4.3.4. *Fuel efficiency and injector limitations*

A deeper evaluation of fuel conversion efficiency was made by comparing the unburnt fuel fraction in the exhaust to the total fuel injected. These results, shown in Table 13, confirm that a substantial portion of the extra kerosene injected in fuel-rich cases left the engine unburnt. For *c98hp*, nearly 18 % of the injected kerosene exited the nozzle without reacting, compared to just under 9 % for the stoichiometric counterpart. This incomplete combustion not only reduced performance but also increased thermal inefficiencies and potential pollutant formation.

4.4. *Wall temperature and structural loading*

Understanding the thermal and mechanical loads on the thruster chamber wall is essential for evaluating the structural viability of the design, particularly under high-temperature, high-pressure operation. While transient peaks during ignition or instability phases can occur in rocket engines, the simulations indicated that such effects were negligible in the current setup. Instead, the steady-state thermal and mechanical loads were found to dominate and thus were the focus of the structural assessment. This approach is justified by the relatively short fluid dynamic start-up phase compared to the longer time required for thermal saturation of the wall structure.

Prior to analyzing wall thermal loads, the quality of the near-wall mesh resolution was assessed using the dimensionless wall distance y^+. Fig. 16 shows the distribution of y^+ obtained in the final simulations. Across most of the combustion chamber, the viscous sublayer was fully resolved ($y^+ < 5$), ensuring direct numerical capture of near-wall gradients without relying on wall functions. In the throat region, y^+ values exceeded 30, placing the first grid point into a fully turbulent region where near-wall velocity gradients are approximated using wall models. The SST k–ω turbulence model was selected for its robustness in handling variable y^+ ranges, blending k–ω near the wall and k–ε away from it. While further refinement in the throat and nozzle regions could improve resolution, the existing setup was deemed sufficient for capturing the dominant thermal and mechanical loading trends.

With the near-wall resolution confirmed to be within acceptable limits, the analysis then focused on evaluating the steady-state wall temperature distributions and their implications for structural integrity.

4.4.1. *Wall temperature distribution*

The maximum allowable temperature for the UHTCMC wall material was set to 2773 K, based on structural reliability limits discussed in Section 2.2. Simulation results revealed that this limit was exceeded by up to 500 K, with peak wall temperatures reaching as high as 3271 K in the reference case (*c98st*). This overshoot was largely attributed to the adiabatic wall boundary condition applied in the model, which assumes no heat dissipation through the wall. While this assumption simplifies numerical treatment and aligns with common practice in early-stage engine simulations, it neglects important cooling pathways such as

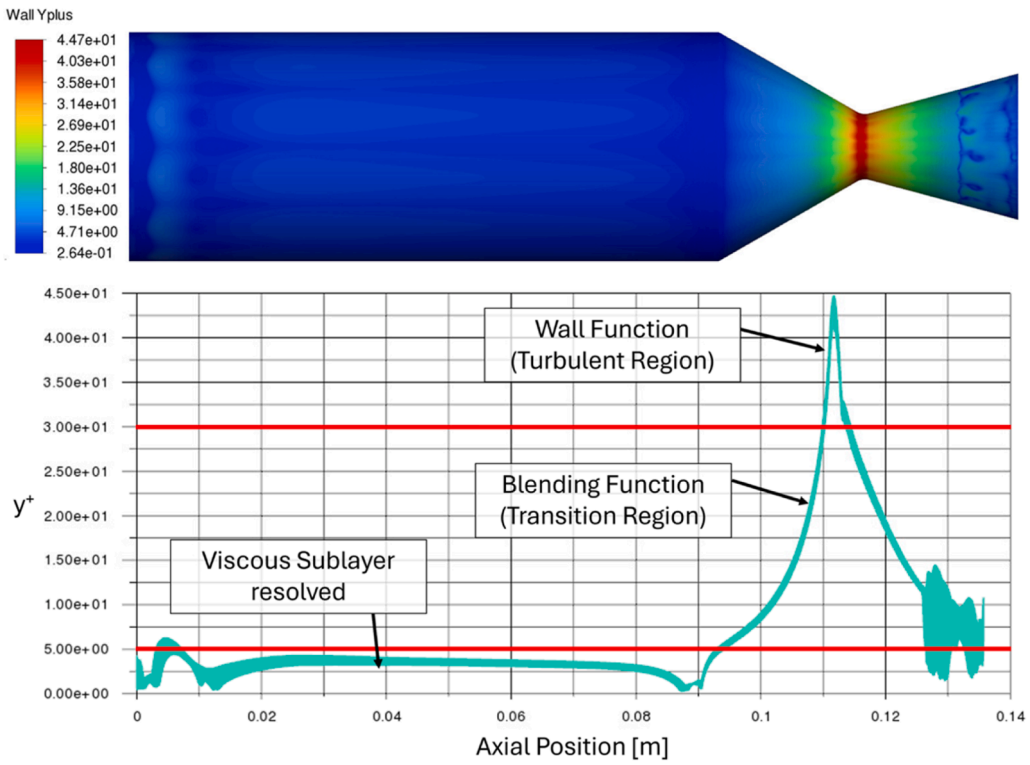

Fig. 16. y^+ 3D contour (top) and plot over axial distance, highlighting different zones (bottom).

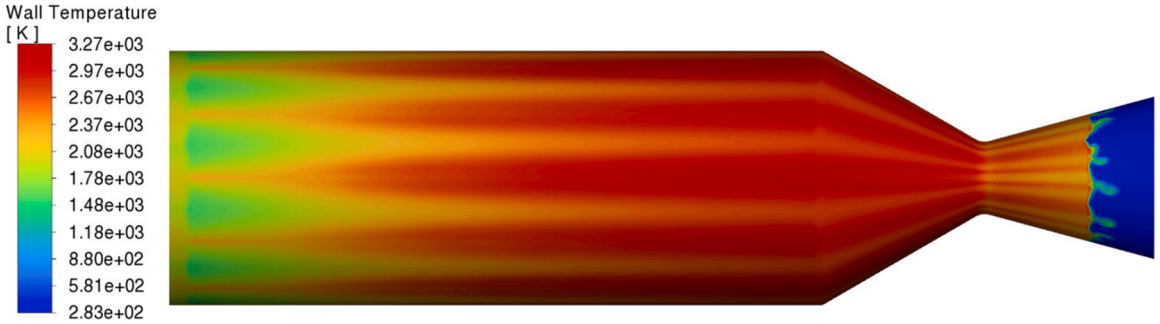

Fig. 17. 3D-contour of temperature on the inside of the chamber wall (c98st).

convective losses to the atmosphere during ground operation and radiative cooling in space. As such, the reported temperatures likely represent conservative overestimates of actual structural loads.

The wall temperature contours, shown in Fig. 17, revealed a distinct circumferential variation that corresponded directly with the injector arrangement. Local hotspots formed near oxidizer injection regions, reinforcing the importance of injector configuration in determining surface heating. More uniform injection, potentially through pintle or impinging-jet designs, could mitigate these peaks. Modifications to the existing coaxial injector, such as shifting propellant flow inward or reducing outer injector elements, may also reduce wall loads without requiring full redesign.

Temperature profiles for all four propellant configurations are shown in Fig. 18. As expected, higher HTP concentrations led to higher wall temperatures, with a maximum variation of about 2 % between 95 % and 98 % HTP. Differences between stoichiometric and fuel-rich mixtures of the same concentration were smaller, typically under 1 %. The axial shift in the location of peak wall temperatures across cases suggests that combustion onset and flow separation varied slightly, depending on how efficiently the fuel and oxidizer mixed, delayed combustion in fuel-rich cases being a likely cause.

4.4.2. *Heat transfer coefficient and thermal flux*

The convective heat transfer coefficient at the wall was computed using the y^+-based estimation, and its axial distribution is plotted in Fig. 19. As expected, the maximum heat transfer occurred at the throat, where flow velocities and thermal gradients are greatest. Before the nozzle, typical heat transfer coefficients were around 750 $W/m^2{\cdot}K$, while peak values at the throat reached 4600 to 4676 $W/m^2{\cdot}K$ across different propellant combinations. The differences between cases were minimal, under 2 %, with the highest value again observed in the fuel-rich 98 % HTP configuration (*c98hp*).

However, a comparison with analytical predictions using Bartz's formula [19,20] revealed that the y^+-based method tends to overestimate the heat transfer coefficient by a factor of two at the throat. This discrepancy is partially due to the elevated y^+ values at the throat region (Fig. 16), indicating insufficient near-wall resolution. Additionally, the assumption of an adiabatic wall may have led to artificially high gas temperatures near the boundary, further inflating the calculated thermal flux. Future work could incorporate non-adiabatic boundary conditions

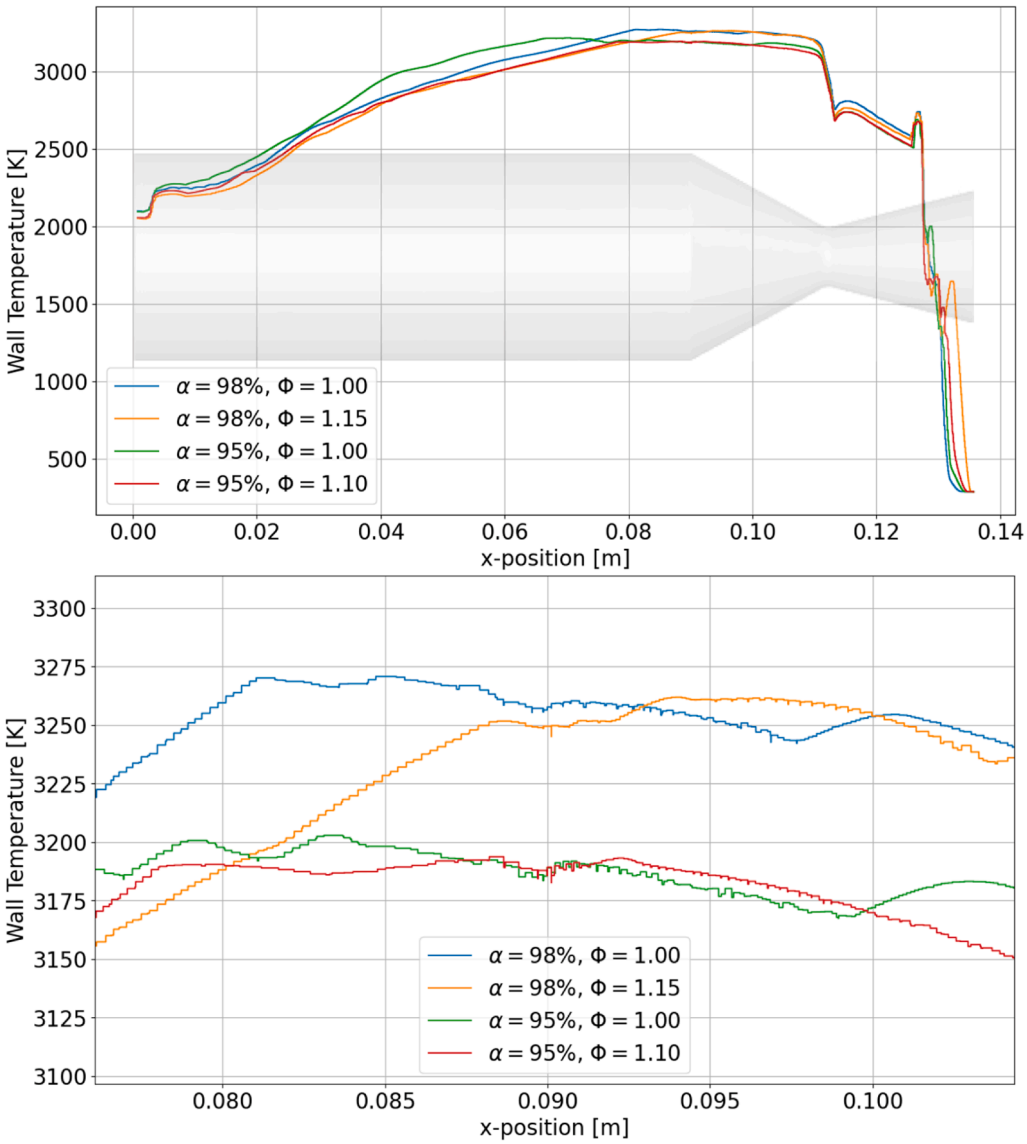

Fig. 18. Wall temperature for different propellants; whole chamber (top) and zoomed nozzle entrance (bottom).

and finer near-wall meshing to improve heat transfer accuracy and better inform cooling system requirements.

4.4.3. *Mechanical loads: shear stress and pressure*

The mechanical stress on the chamber wall was evaluated through two key quantities, i.e., wall shear stress and static pressure. Wall shear stress peaked in the throat region, ranging from 2471 Pa (*c98hp*) to 2506 Pa (*c98st*) across the configurations, as shown in Fig. 20. These values closely followed the velocity gradient, as shear stress is directly proportional to the rate of momentum change at the wall. The relatively small variation (1.4 %) again highlights that mixture ratio, and concentration had a modest influence on mechanical stress when injector and geometry remained constant.

The static pressure remained nearly uniform throughout the chamber, consistent with the relatively low axial flow velocities prior to the throat (as discussed in Section 4.2.2). The maximum static pressures ranged between 7.54 bar and 7.66 bar, corresponding to 6.53–6.65 bar in gauge pressure, assuming atmospheric conditions for ground testing. For space applications, where ambient pressure approaches zero, these values represent the total differential pressure across the wall, critical for structural dimensioning and safety margin calculation. While pressure loading was relatively steady and well-distributed, the thermal stresses introduced by high wall temperatures, especially near the throat and injector regions, pose a greater concern for material survivability. The combination of peak mechanical and thermal loads underscores the need for both advanced material systems like UHTCMC and carefully engineered injector arrangements to optimize both performance and durability.

4.5. *Verification and theoretical comparison*

Although direct experimental validation of the transient simulations was not available during this phase of the research, extensive cross-verification with analytical models and theoretical predictions was performed. This section benchmarks the simulation results against thermochemical predictions obtained using NASA CEA calculations, analytical estimates based on established engineering correlations (such as Bartz's formula), and expected physical behavior observed in supersonic nozzle flows. Together, these comparisons offer a strong basis for evaluating the credibility and predictive quality of the simulation framework.

4.5.1. *Verification against CEA thermochemical predictions*

The first level of verification involved comparing key performance

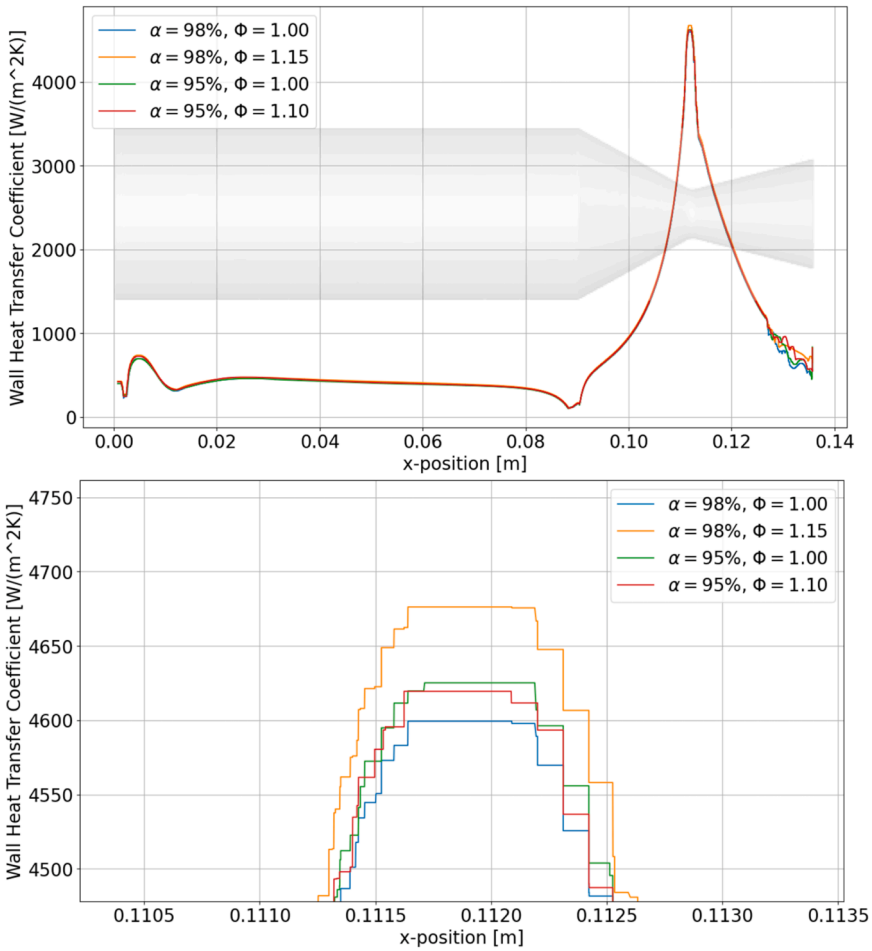

Fig. 19. Conductive y^+-based Wall Heat Transfer Coefficient for different propellants; whole chamber (top) and zoomed throat (bottom).

metrics, such as maximum chamber temperature, specific impulse (I_{sp}), and chamber pressure, between the simulations and theoretical predictions from CEA. Table 14 summarizes these comparisons for all four propellant combinations.

The deviations between simulated and predicted maximum temperatures were within ±3 %, and specific impulse deviations were under 1.5 %, indicating very strong agreement considering that CEA assumes perfect chemical equilibrium, while the simulations modeled finite-rate chemistry and real-gas effects. Minor deviations in pressure were expected due to combustion inefficiencies and wall heat losses not captured by equilibrium codes.

4.5.2. *Wall heat transfer comparison using bartz's correlation*

Heat transfer predictions at the chamber wall, particularly near the throat where thermal loading peaks, were verified against estimates obtained using Bartz's empirical formula [19,20]. Table 15 presents a comparison between the throat heat fluxes estimated from Bartz's method and those computed from the simulation using the y^+-based wall heat transfer coefficient.

The simulation results overestimated heat fluxes by approximately a factor of two relative to Bartz's prediction. This discrepancy can be attributed to:

- High wall-adjacent gas temperatures resulting from the adiabatic boundary condition.
- Elevated y^+ values near the throat, reducing near-wall gradient resolution.
- Simplified assumptions in Bartz's model regarding gas properties and flow uniformity.

While the absolute values differed, the trends between cases were consistent, with higher heat flux observed for higher concentration and richer fuel mixtures, correlating correctly with higher combustion temperatures.

4.5.3. *Physical consistency checks: flow structures and ignition behavior*

Table 16 summarizes key findings from the simulations, comparing them with expected physical behaviors commonly observed in similar thruster flows. These behaviors include shock diamond formation, flow separation, ignition timing, and combustion efficiency trends. The results show a good alignment with theoretical expectations, particularly regarding shock-expansion structures, nozzle flow separation, and the effects of fuel-rich mixtures on combustion efficiency. However, ignition timing was aligned with the range of IDTs reported by researchers in studies [6,21] over similar engines.

Thus, the flow field development, ignition behavior, shock patterns, and exhaust species composition all reinforced the physical practicality of the simulated engine performance.

4.6. *Limitations of the study*

It is important to acknowledge the limitations of this numerical study. First, the adiabatic wall boundary condition leads to a conservative overprediction of wall temperatures. Simulation results indicate peak temperatures approximately 500 K above the material safety limit. In a flight-ready engine, radiative and convective cooling to the environment would significantly lower these peaks. While this assumption provides a robust "worst-case" load for structural dimensioning, it does not reflect the thermal equilibrium of an operational mission.

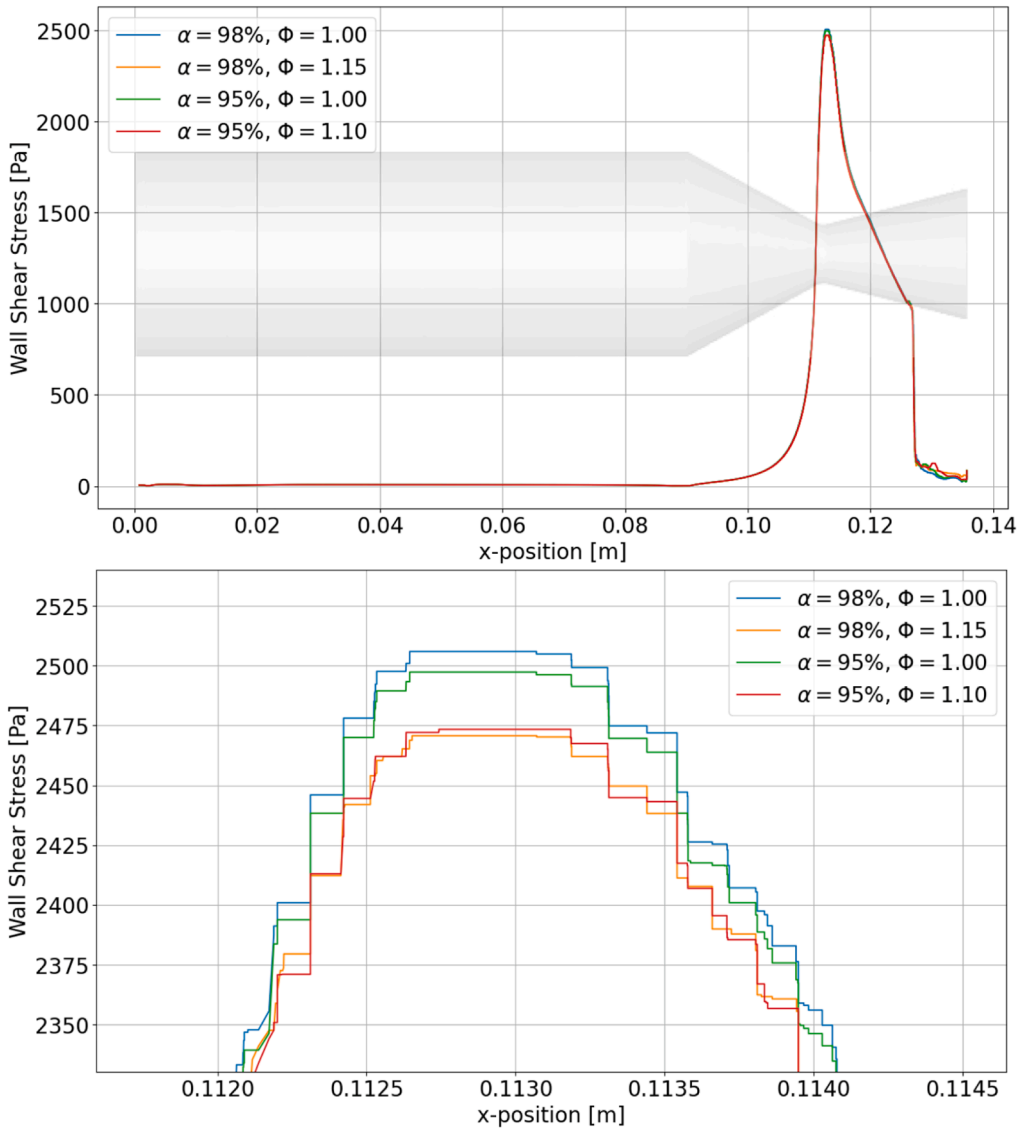

Fig. 20. Wall Shear Stress for different propellants; whole chamber (top) and zoomed nozzle entrance (bottom).

Table 14
Comparison of simulation results with CEA predictions.

Case	Parameter	CEA Prediction	Simulation Result	Deviation (%)
α = 98 %, Φ = 1.00	Max Temp [K]	2787	2806	+0.68 %
	Specific Impulse [s]	277.4	280.3*	+1.04 %
	Chamber Pressure [bar]	7.50	7.66	+2.13 %
α = 98 %, Φ = 1.15	Max Temp [K]	2740	2758	+0.66 %
	Specific Impulse [s]	279.4	278.2*	−0.43 %
α = 95 %, Φ = 1.00	Max Temp [K]	2763	2682	−2.93 %
α = 95 %, Φ = 1.10	Max Temp [K]	2724	2666	−2.13 %

(*Specific impulse derived from thrust and mass flow simulations)

Table 15
Comparison of wall heat flux predictions.

Case	Throat Heat Flux – Bartz [W/m^2]	Simulated Wall Heat Flux [W/m^2]	Deviation (%)
α = 98 %, Φ = 1.00	2200	4600	+109 %
α = 98 %, Φ = 1.15	2250	4676	+108 %

Second, the chemical kinetics model employs a reduced three-step global mechanism. While this approach is computationally efficient and sufficient for capturing macroscopic heat release and pressure trends, it does not resolve intermediate species or radical formation as fully as detailed elementary mechanisms would. Additionally, the use of constant Arrhenius parameters over the entire temperature range represents a simplification; while valid for the high-temperature combustion regime that drives the primary thermal loads, this may introduce uncertainties during the low-temperature induction phase. Furthermore, the catalyst effect was modeled implicitly by modifying Arrhenius rate parameters rather than by simulating catalyst transport or surface chemistry. Finally, this study relies on high-fidelity numerical predictions verified against theoretical models (CEA, Bartz). Direct experimental validation of the specific transient ignition profiles presented here was outside the scope of this work and is the subject of parallel experimental investigations.

Table 16
Comparison of simulation results with expected physical behaviors in thruster flows.

Simulation Aspect	Observation	Comparison with Expected Behavior
Shock Diamond Formation	Repeated shock-expansion structures (shock diamonds) observed in the nozzle plume after t ≈ 20 ms.	Consistent with over-expanded flow at sea-level backpressure.
Flow Separation	Flow separation at the nozzle wall detected around t ≈ 10–15 ms.	Matches expectations for engines optimized for vacuum expansion operating at ground pressure.
Ignition Timing	Ignition occurred at approximately 7 ms after injection start.	Matches with similar reported engines having an IDT between 4 ms and 17 ms and a time to steady-state of 80 ms, confirming the order of magnitude of the startup time.
Combustion Efficiency Trends	Fuel-rich mixtures resulted in incomplete combustion, lower temperatures, and thrust.	Consistent with classical propulsion theory: excessive fuel impairs flame temperature and combustion.

5. Conclusion

In this study, a high-fidelity, transient CFD framework was developed to comprehensively simulate and analyze the ignition, combustion, and structural response of a bipropellant thruster using high-test hydrogen peroxide (HTP) with kerosene. Detailed droplet-phase modeling, finite-rate chemical kinetics, and real-gas thermodynamics were integrated to capture the intricate fluid-thermal-chemical interactions. Simulations covering different oxidizer concentrations (95 % and 98 %) and mixture ratios (stoichiometric and slightly fuel-rich) revealed that stoichiometric operation with 98 % HTP offered the best balance between combustion efficiency and material survivability. Peak chamber temperatures reached 2806 K, closely matching CEA predictions with deviations under 1 %, while thrust values (~63 N sea-level equivalent) exhibited less than 2 % variance across propellant conditions. Fuel-rich mixtures, although theoretically offering higher I_{sp}, demonstrated significant incomplete combustion (up to 17.5 % unburnt fuel) and elevated wall thermal loading. Wall temperatures exceeded safe UHTCMC limits under adiabatic assumptions, with peak values near 3270 K, underscoring the critical need for active or passive cooling strategies. The verification against analytical models, combined with the identification of flow separation, shock diamonds, and exhaust species trends, confirmed the model's physical robustness. Overall, this work not only bridges the transient combustion-structural coupling for green bipropellant systems but also establishes a foundation for optimizing injector designs and propellant formulations toward operational HTP-kerosene thrusters suitable for environmentally compliant aerospace applications.

Data availability statement

The data that support the findings of this study are available from the corresponding author upon reasonable request.

CRediT authorship contribution statement

Prakhar Jindal: Writing – original draft, Visualization, Validation, Supervision, Software, Resources, Project administration, Methodology, Funding acquisition, Data curation, Conceptualization. **Maximilian Pfohl:** Writing – review & editing, Visualization, Validation, Software, Methodology, Investigation, Formal analysis, Conceptualization. **Jyoti Botchu:** Writing – review & editing, Supervision, Project administration.

Declaration of competing interest

The authors declare the following financial interests/personal relationships which may be considered as potential competing interests:

Prakhar Jindal reports financial support was provided by Horizon Europe. If there are other authors, they declare that they have no known competing financial interests or personal relationships that could have appeared to influence the work reported in this paper.

Acknowledgements

This material is based upon the work supported by Horizon Europe's research and innovation programme under the Marie Sklodowska-Curie grant agreement No. 101107214. The authors acknowledge the extensive support from the Space System Engineering section of the Faculty of Aerospace Engineering, Delft University of Technology, Netherlands.

References

[1] T. Haas, H. Sander, Decarbonizing transport in the European Union: emission performance standards and the perspectives for a European green deal, Sustainability 12 (2020) 8381, https://doi.org/10.3390/su12208381.
[2] C.M. Lousada, A.J. Johansson, T. Brinck, M. Jonsson, Mechanism of H 2 O 2 decomposition on transition metal oxide surfaces, J. Phys. Chem. C 116 (2012) 9533–9543, https://doi.org/10.1021/jp300255h.
[3] C.M. Lousada, M. Yang, K. Nilsson, M. Jonsson, Catalytic decomposition of hydrogen peroxide on transition metal and lanthanide oxides, J. Mol. Catal. Chem. 379 (2013) 178–184, https://doi.org/10.1016/j.molcata.2013.08.017.
[4] N.R. Council, Levels C on AEG, Hydrazine Acute Exposure Guideline Levels. Acute Exposure Guideline Levels for Selected Airborne Chemicals: Volume 8, National Academies Press, US), 2010.
[5] E. Croiset, S.F. Rice, RG. Hanush, Hydrogen peroxide decomposition in supercritical water, AIChE J. 43 (1997) 2343–2352, https://doi.org/10.1002/aic.690430919.
[6] H. Kang, D. Jang, S. Kwon, Demonstration of 500 N scale bipropellant thruster using non-toxic hypergolic fuel and hydrogen peroxide, Aerosp. Sci. Technol. 49 (2016) 209–214, https://doi.org/10.1016/j.ast.2015.11.038.
[7] Bonifacio S, Russo A. Modelling hydrogen peroxide decomposition in monolithic beds 2006.
[8] R. Amrousse, R. Brahmi, Y. Batonneau, C. Kappenstein, Thermal and catalytic decomposition of H2O2-ionic liquid monopropellant mixtures on monolith-based catalysts. 46th AIAA/ASME/SAE/ASEE Joint Propulsion Conference & Exhibit, American Institute of Aeronautics and Astronautics, Reston, Virigina, 2010, https://doi.org/10.2514/6.2010-6983.
[9] I. Müller, M. Kuhn, I. Petkov, S. Bletsch, K. Huybrechts, P. Van Cauwenbergh, 3D-Printed coaxial injector for a lox/kerosene rocket engine, Space Propuls. 2018 (2018).
[10] S-H Do, B. Batchelor, H-K Lee, S-H. Kong, Hydrogen peroxide decomposition on manganese oxide (pyrolusite): kinetics, intermediates, and mechanism, Chemosphere 75 (2009) 8–12, https://doi.org/10.1016/j.chemosphere.2008.11.075.
[11] D. Jang, S. Kang, S. Kwon, Preheating characteristics of H2O2 monopropellant thruster using manganese oxide catalyst, Aerosp. Sci. Technol. 41 (2015) 24–27, https://doi.org/10.1016/j.ast.2014.12.010.
[12] S. Jo, S. An, J. Kim, H. Yoon, S. Kwon, Performance characteristics of hydrogen peroxide/kerosene staged-bipropellant engine with axial fuel injector, J. Propuls. Power. 27 (2011) 684–691, https://doi.org/10.2514/1.B34083.
[13] G. Sabiston, Plasma-Infusion for Advanced Materials in Space Propulsion and Fusion Energy, University of California, Los Angeles, 2024.
[14] E. Fonda-Marsland, G. Roberts, D. Gibbon, C. Ryan, Development of a low-cost 0.1N high test peroxide thruster using additive manufacturing. AIAA Propulsion and Energy 2019 Forum, American Institute of Aeronautics and Astronautics, Reston, Virginia, 2019, https://doi.org/10.2514/6.2019-4227.
[15] F. Kerstens. Preliminary design of a small hydro-gen peroxide cooled thrust chamber for additivemanufacturing, 2015.
[16] A. Coclite, L. Cutrone, G. Pascazio, P. De Palma, Numerical investigation of high-pressure combustion in rocket engines using Flamelet/Progress-variable models.

53rd AIAA Aerospace Sciences Meeting, American Institute of Aeronautics and Astronautics, Reston, Virginia, 2015, https://doi.org/10.2514/6.2015-1109.
[17] X. Wang, L. Zhang, Y. Li, S-T Yeh, V. Yang, Supercritical combustion of gas-centered liquid-swirl coaxial injectors for staged-combustion engines, Combust. Flame 197 (2018) 204–214, https://doi.org/10.1016/j.combustflame.2018.07.018.
[18] P. ROSIN, The laws governing the fineness of powdered coal, J. Inst. Fuel 7 (1933) 29–36.
[19] B.T.C. Zandbergen. Thermal Rocket Propulsion, TUDelft, 2025 version 2.10.
[20] R. BD, A simple equation for rapid estimation of rocket nozzle convective heat transfer coefficients, Jet. Propul. 27 (1957) 49–51.
[21] B.L. Austin, S.D. Heister, WE. Anderson, Characterization of Pintle engine performance for nontoxic hypergolic bipropellants, J. Propuls. Power 21 (2005) 627–635, https://doi.org/10.2514/1.7988.